Defense Threat Reduction Agency
8725 John J. Kingman Road, MS
6201 Fort Belvoir, VA 22060-6201

DTRA-TR-19-5

TECHNICAL REPORT

Fragmentation of Solid Materials Using Shock Tubes Part 4: Second Test Series in a Large-Diameter Shock Tube

January 2019

HDTRA1-14-C-0001

Bryan Bewick et al.

Prepared by:
Protection Engineering Consultants
SRI International
Engility Corp.

DESTRUCTION NOTICE:

Destroy this report when it is no longer needed.
Do not return to sender.

PLEASE NOTIFY THE DEFENSE THREAT REDUCTION AGENCY, ATTN: DTRIAC/ RD-NTF, 8725 JOHN J. KINGMAN ROAD, MS-6201, FT BELVOIR, VA 22060-6201, IF YOUR ADDRESS IS INCORRECT, IF YOU WISH IT DELETED FROM THE DISTRIBUTION LIST, OR IF THE ADDRESSEE IS NO LONGER EMPLOYED BY YOUR ORGANIZATION.

REPORT DOCUMENTATION PAGE

Form Approved
OMB No. 0704-0188

1. REPORT DATE *(DD-MM-YYYY)*	**2. REPORT TYPE**	**3. DATES COVERED** *(From - To)*
00-01-2019	Technical	N/A

4. TITLE AND SUBTITLE

Fragmentation of Solid Materials Using Shock Tubes Part 4: Second Test Series in a Large-Diameter Shock Tube

5a. CONTRACT NUMBER
HDTRA1-14-C-0001

5b. GRANT NUMBER

5c. PROGRAM ELEMENT NUMBER

6. AUTHOR(S)

Bryan Bewick (a), Greg Rolater (a), Kirk Marchand (a), Adam Ziemba (b), Mohsen Sanai (b) and Culbert Laney (c)

5d. PROJECT NUMBER

5e. TASK NUMBER

5f. WORK UNIT NUMBER

7. PERFORMING ORGANIZATION NAME(S) AND ADDRESS(ES)

(a) Protection Engineering Consultants, PO Box 781607, San Antonio, TX 78278
(b) SRI International, 333 Ravenswood Ave., Menlo Park, CA 94025
(c) Engility Corporation, 8211 Terminal Road, Suite 1000, Lorton, VA 22079

8. PERFORMING ORGANIZATION REPORT NUMBER

9. SPONSORING / MONITORING AGENCY NAME(S) AND ADDRESS(ES)

Defense Threat Reduction Agency
8725 John J. Kingman Road, STOP 6201
Fort Belvoir, VA 22060-6201

10. SPONSOR/MONITOR'S ACRONYM(S)
DTRA

11. SPONSOR/MONITOR'S REPORT NUMBER(S)
DTRA-TR-19-5

12. DISTRIBUTION / AVAILABILITY STATEMENT

Distribution Statement A. Approved for public release; distribution is unlimited.

13. SUPPLEMENTARY NOTES

14. ABSTRACT

This report describes a series of tests that used an explosively-driven large-diameter shock tube to shatter an 8-ft x 8-ft brick wall, an 8-ft x 8-ft x 5-in reinforced concrete structural panel, an 8-ft x 8-ft x 4-in reinforced concrete spandrel panel, and an 8-ft x 8-ft clay tile roof using relatively low-pressure, long-duration blast loads. All four tests obtained power law size distributions with exponents between –0.80 and –1.07. The results are comparable to those obtained in earlier tests, including a test involving an 8-ft x 8-ft cinder block wall, and a test series involving small-scale simply-supported plates composed of glass, concrete, and masonry.

15. SUBJECT TERMS

debris, breakage, fragmentation, long-duration blast, shock tubes, reinforced concrete panels, unreinforced masonry walls,

16. SECURITY CLASSIFICATION OF:			**17. LIMITATION OF ABSTRACT**	**18. NUMBER OF PAGES**	**19a. NAME OF RESPONSIBLE PERSON**
a. REPORT	**b. ABSTRACT**	**c. THIS PAGE**			MAJ David Matters
U	U	U	UU	54	**19b. TELEPHONE NUMBER** *(include area code)* 571-616-5217

Standard Form 298 (Rev. 8-98)
Prescribed by ANSI Std. Z39.18

UNIT CONVERSION TABLE

U.S. customary units to and from international units of measurement*

U.S. Customary Units	Multiply by → / ← Divide by†		International Units
Length/Area/Volume			
inch (in)	2.54	$\times 10^{-2}$	meter (m)
foot (ft)	3.048	$\times 10^{-1}$	meter (m)
yard (yd)	9.144	$\times 10^{-1}$	meter (m)
mile (mi, international)	1.609 344	$\times 10^{3}$	meter (m)
mile (nmi, nautical, U.S.)	1.852	$\times 10^{3}$	meter (m)
barn (b)	1	$\times 10^{-28}$	square meter (m^2)
gallon (gal, U.S. liquid)	3.785 412	$\times 10^{-3}$	cubic meter (m^3)
cubic foot (ft^3)	2.831 685	$\times 10^{-2}$	cubic meter (m^3)
Mass/Density			
pound (lb)	4.535 924	$\times 10^{-1}$	kilogram (kg)
unified atomic mass unit (amu)	1.660 539	$\times 10^{-27}$	kilogram (kg)
pound-mass per cubic foot (lb ft^{-3})	1.601 846	$\times 10^{1}$	kilogram per cubic meter (kg m^{-3})
pound-force (lbf avoirdupois)	4.448 222		newton (N)
Energy/Work/Power			
electron volt (eV)	1.602 177	$\times 10^{-19}$	joule (J)
erg	1	$\times 10^{-7}$	joule (J)
kiloton (kt) (TNT equivalent)	4.184	$\times 10^{12}$	joule (J)
British thermal unit (Btu) (thermochemical)	1.054 350	$\times 10^{3}$	joule (J)
foot-pound-force (ft lbf)	1.355 818		joule (J)
calorie (cal) (thermochemical)	4.184		joule (J)
Pressure			
atmosphere (atm)	1.013 250	$\times 10^{5}$	pascal (Pa)
pound force per square inch (psi)	6.984 757	$\times 10^{3}$	pascal (Pa)
Temperature			
degree Fahrenheit (^oF)	$[T(^oF) - 32]/1.8$		degree Celsius (^oC)
degree Fahrenheit (^oF)	$[T(^oF) + 459.67]/1.8$		kelvin (K)
Radiation			
curie (Ci) [activity of radionuclides]	3.7	$\times 10^{10}$	per second (s^{-1}) [becquerel (Bq)]
roentgen (R) [air exposure]	2.579 760	$\times 10^{-4}$	coulomb per kilogram (C kg^{-1})
rad [absorbed dose]	1	$\times 10^{-2}$	joule per kilogram (J kg^{-1}) [gray (Gy)]
rem [equivalent and effective dose]	1	$\times 10^{-2}$	joule per kilogram (J kg^{-1}) [sievert (Sv)]

*Specific details regarding the implementation of SI units may be viewed at http://www.bipm.org/en/si/.

†Multiply the U.S. customary unit by the factor to get the international unit. Divide the international unit by the factor to get the U.S. customary unit.

EXECUTIVE SUMMARY

The report describes the last of four test series designed to help develop a probabilistic, physics-based model for the fragmentation of building components subjected to airblast. Like the second test series, the primary objective of this test series was to explore how conventional façade wall components fragment under relatively long duration, low pressure loads. A secondary objective was to explore how the façade material – brick, concrete, tile – affected fragment size distributions.

A large-diameter explosively-driven shock tube was employed to produce the desired low pressure, long duration loads. The shock tube was driven by long line charges of Primacord and spaced packets of Unigel.

Four full-scale samples were tested in this series, namely, an 8-ft x 8-ft brick wall, an 8-ft x 8-ft x 5-in reinforced concrete structural panel, an 8-ft x 8-ft x 4-in reinforced concrete spandrel panel, and an 8-ft x 8-ft clay tile roof, each carefully fabricated and mounted to replicate real-world construction techniques.

The fragment size distributions were estimated by physically collecting fragments. Over 100,000 fragments were collected in each test. As in previous tests, the fragments collected were sieved into size bins. However, unlike previous tests, no attempt was made to characterize the entire set of fragments. Instead, to reduce time and expense, two random 5% samples were taken from each size bin. If the results of the two random samples agreed, which was approximately true in all cases, they were combined to form a single 10% random sample.

All four tests in this series obtained power law size distributions with exponents between –0.80 and –1.07. These results are compared to those obtained in the previous test series. In particular, the results are comparable those obtained in the second test series, which used a large-diameter explosively-driven shock tube to shatter an 8-ft x 8-ft cinder block wall. In addition, the results are comparable to those obtained in the third test series, which used a small-diameter, explosively-driven shock tube to shatter small-scale simply-supported plates made of glass, concrete, and masonry.

Fragments tend to form in two stages: a short initial stage dominated by rapid random crack formation and propagation; and an extended final stage dominated by high-speed collisions. Based on a review of the results of all four test series, we conclude that fragment size distributions depend on which of these two stages dominates.

Contents

Figures

Tables

1 INTRODUCTION

This report is the last in a four part series:

- Part 1 / Test Series 1 [1]. Measured fragment size distributions, velocity size distributions, and the time-dependency of fragment size distributions in a large number of different small-scale tests involving glass, concrete, and concrete masonry unit (CMU) test articles. The first test series included a fragment stripper that confined fragments to a single focal plane. This allowed for measurements of mid-air fragment size and velocities using a single side-view camera. However, it dramatically reduced the number of fragments captured in a soft-catch collection device, and altered the size distributions of those fragments. Thus the fragment stripper was removed from all subsequent tests.
- Part 2 / Test Series 2 [2]. Measured fragment size distributions in a small number of different large-scale tests involving plate glass windows, concrete panels, and CMU walls. These tests showed that, for plate glass and perhaps other materials, the size distributions obtained at small scales in Part 1 also occur at large scales.
- Part 3 / Test Series 3 [3]. Measured fragment size distributions in a large number of different small-scale tests involving glass, concrete, and CMU test articles. Compared to the first test series, the third test series explored a wider range of loads, sample strengths, and sample thicknesses. In addition, because the fragment stripper was removed, the third test series captured a much large number of fragments. The soft-catch fragment collection device had to be redesigned to survive the higher overpressures used in this test series.
- Part 4 / Test Series 4 *(this report)*. Measured fragment size distributions in a small number of different large-scale tests involving brick walls, concrete panels, and clay tile roofs. Building on Part 2, this test series provided further evidence that the size distributions obtained at small scales in Parts 1 and 3 also occur at large scales.

All of these tests used explosively-driven shock tubes. Shock tubes have rarely, if ever, been used to systematically study fragment size and velocity distributions prior to this work. However, shock tubes have often been used to study related issues such as breakage thresholds, breakage times, and debris throw distances; see, e.g., [4] [5] [6].

SRI International built and operates two shock tubes, one large and one small, driven by extended line charges of explosive that can produce sustained high overpressures typical of certain real-world events. Both shock tubes are located at SRI's Corral Hollow Experimental Site (CHES). The loads generated by a shock tube must, to some extent, balance peak overpressure with duration. Earlier test series in SRI's small shock tube favored larger peak overpressures with shorter durations [1] [3]. However, like the second test series [2], this test series in SRI's large shock tube favored larger durations but with smaller peak overpressures. More specifically, the peak static overpressures obtained in the large shock tube were two orders-of-magnitude lower, and the positive phase durations were one order-of-magnitude higher, than those obtained in the small shock tube. In such cases, the structural components fail primarily due to flexure, as opposed to the high-strain-rate crushing or impact-type failures that occur at higher overpressures.

In Test Series 2 and 4, samples were chosen based on their prevalence in U. S. and foreign construction practices. Researchers have previously studied fragmentation of brick walls (e.g., [4] [7]), CMU walls (e.g. [8] [9] [10] [11]), concrete panels (e.g., [11] [12]), and especially plate glass

windows (e.g., [5] [6] [8]). However, researchers have rarely studied fragmentation of clay tile roofs, as in this test series, despite the fact they are commonly found on buildings worldwide.

Based on a survey of legacy test results, "reinforced concrete slabs do not constitute a significant source of debris … The steel reinforcing bars tenaciously tie the various pieces of fractured slab to the supports and to each other even at pressure levels as high as 100 psi." [12]. While this is consistent with our experience in Test Series 2 [2], this test series used different mounting techniques, reinforcing materials, panel thicknesses, and especially concrete strengths. As a result, the two concrete panels tested in this series produced a significant number of high-speed fragments, even though the majority of each panel remained relatively intact.

2 TEST SETUP

2.1 TEST MATRIX

Table 1 shows the text matrix used for this test series. As in previous tests, SRI operated the shock tube and fielded the measurement equipment, such as the Kulite strain gages and high-speed video cameras, while Protection Engineering Consultants (PEC) designed, fabricated and delivered the test specimens, and analyzed the test results, including the fragment size distributions.

Table 1. Test Matrix.

Test	Date	Time	Sample Type	Sample Weight (lbs.)	Charge Weight (lbs.)	Temp. (°F)	Atmos. Press. (psia)	Sound Speed (m/s)	Peak Static Ovepress. (psi)	Positive Phase Duration (ms)	Impulse (psi-ms)
40	11/11/15	15:45	Brick wall	2,670	43.75	52.2	14.22	338	46.8	~100	1,572
41	11/16/15	13:25	Concrete panel	3,980	43.75	52.0	14.17	338	41.3	~100	1,615
42	11/19/15	13:10	Concrete panel	3,180	43.75	59.9	14.13	341	47.2	~100	1,655
43	11/24/15	11:30	Clay tile roof	680	43.75	52.7	13.99	338	47.4	~65	604

2.2 TEST SAMPLES

Table 2 shows the properties of the four samples tested in this series.

Table 2. Sample properties.

Test	Description	Dimensions	Weight (lbs.)	Compressive Strength (psi)	Notes
40	Brick wall	8'x8'x3.625"	2,670	8,640	Compressive strength is for individual bricks.
41	Reinforced concrete structural panel	95"x95"x5"	3,980	4,000[1]	Reinforced with rebar and supported top and bottom.
42	Reinforced concrete spandrel panel	95"x95"x4"	3,180	4,000[1]	Reinforced with a welded wire sheet and supported midspan.
43	Clay tile roof	8'x8'	680	7,940	Compressive strength is for individual tiles.

1. Both concrete panels were fabricated from the same 4,000 psi concrete batch. Concrete cylinders were tested at 7, 14, and 28 days after pour to evaluate the unconfined compressive strength (UCS).

For Test 40, the brick wall used was constructed using a single course of standard facing bricks, with nominal dimensions of 3 5/8" x 2 1/4" x 8", placed in a running bond pattern using Type S mortar. The brick wall was built into an 8-ft-square steel frame that was bolted to a 1-in.-thick steel plate at the end of the shock tube. Figure 1 shows the rear of the brick wall just prior to testing.

Figure 1. Rear view of the brick wall sample used in Test 40.

For Test 41, the concrete structural panel was constructed by placing a reinforcing mat at the panel mid-thickness with #4-bars spaced 22-in vertically and 18-in horizontally. The panel was connected to an 8-ft-square steel frame by three 3/8-in A36 clip angles at the top and bottom. The clip angles were bolted to the frame and embedded in the panel. Figure 2 shows the rear of the reinforced concrete structural panel just prior to testing.

Figure 2. Rear view of the reinforced concrete structural panel sample used in Test 41.

For Test 42, the concrete spandrel was constructed by placing a 4x4–W4.0xW4.0 welded wire sheet at the panel mid-thickness. The panel was connected to an 18" x 6" x ½" hollow structural steel (HSS) spandrel beam, which supported the panel at mid-height. Three 3/8-in A36 clip angles were welded to the bottom of the spandrel beam along one leg and embedded into the concrete panel along the other. Figure 3 shows the rear of the reinforced concrete spandrel panel just prior to testing.

Figure 3. Rear view of the reinforced concrete spandrel panel sample used in Test 42.

Test 43 used Niles Interlocking French clay tiles manufactured by Joe Pessagno & Sons. To capture typical aging effects, these tiles were vintage New Old Stock (NOS) sourced from Enterprise Roofing Inc. located in Concord CA. As seen in Figure 4, the dimensions of each tile were approximately 16-in x 8-1/2-in. The thickness of each tile varied between 3/8-in and 1-1/18-in. These profiled, interlocking tiles had static breaking loads averaging 254-lbs and static compressive strengths averaging 7,940-psi.

Figure 4. Bottom view of the interlocking clay tile used in Test 43.

The tile roof was constructed with a 4/12 pitch with the clay tiles bedded in mortar on top of 5/8-in Oriented Strand Board (OSB) sheathing. The roof was mounted on a frame constructed from heavy steel angle material and placed on the test pad outside of the shock tube. The heavy steel frame was fixed in place by bolting it to the 8-ft opening of the shock tube on one end and by welding angles from the steel roof frame to the concrete pad on the other end. This design allowed the roof to flex while the heavy steel frame remained rigid. Figure 6 shows two views of the clay tile roof immediately prior to testing.

Figure 5. Pre-test views of the clay tile roof sample used in Test 43.

2.3 SHOCK TUBE

Figure 6 shows the large-diameter shock tube used in this test series. The shock tube consists of a 258-ft-long, 8-ft-diameter steel tube with a 10-ft-long expansion cone that increases the exit diameter to 12 ft. A concrete floor runs for 246 ft from the driver end at a height of 2 ft from the bottom of the shock tube before sloping down in the final 12 ft to meet the cone extension.

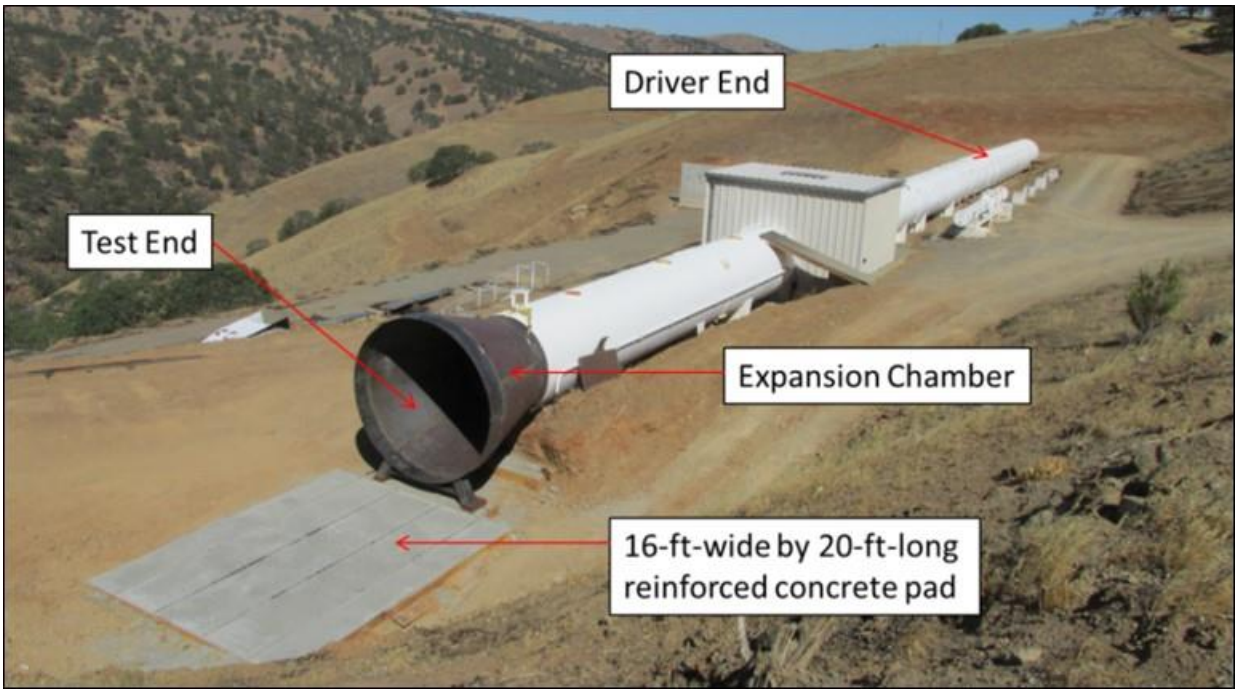

Figure 6. Shock tube used in this test series.

Figure 7 shows the large diameter shock tube immediately prior to a test with the test sample and measurement equipment in place. In the first three tests, the test sample was attached to an 8-ft-square opening at the end of the cone. The driver end of the shock tube was closed by a steel plate backed by concrete blocks. The exit end was closed by the test specimen. In the last test, the test sample was attached to the bottom of the 8-ft-square opening, such that the clay tile roof extended away from the shock tube at a 12:4 riser angle, leaving the shock tube exit open.

Figure 7. Shock tube with a test sample and measurement equipment in place.

2.4 EXPLOSIVE DRIVER

The same explosive driver was used for all four tests in this series. As seen in Figure 8, the explosive driver was a suspended line charge composed of 35 Unigel packets (TNT, 2-in.-diameter by 8-in.-long, 1.15-lb net explosive weight) taped to an 80-ft-long strand of Primacord (200-grain/ft) and placed near the centerline of the shock tube at the driver end. The Unigel packets (detonation velocity ~4,300 m/s) were side-detonated with the Primacord strand (detonation velocity ~6,700 m/s), with the detonation wave traveling upstream away from the test end of the shock tube toward the closed driver end.

Figure 8. Photograph of the explosive driver inside the shock tube.

Table 3 shows the configuration of the Unigel packets and Primacord strand. For more information on using explosive line charges to drive shock tubes see, e.g., Reference [13].

Table 3. Explosive driver characteristics.

Distance from driver end	80 – 64 ft.	64 – 48 ft.	48 – 32 ft.	32 – 8 ft.	8 – 0 ft.
Spacing between Unigel packets.	1 / 9.6-in.	1 / 2-ft	1 / 4-ft	1 / 8-ft	Primacord only
Number of Unigel charges	20	8	4	3	0
Number of Unigel charges per 8-ft section	10	4	2	1	0
Weight of Unigel and Primacord	23.5 lb	9.66 lb	5.06 lb	4.14 lb	1.38 lb
Average linear density of Unigel and Primacord	1.47 lb/ft	0.60 lb/ft	0.32 lb/ft	0.17 lb/ft	0.03 lb/ft

2.5 INSTRUMENTATION

Eight pressure gages were installed inside the shock tube to measure pressure-histories of the shock wave as it traveled the down tube toward the test specimen. Single gages were located at standoffs of 166 ft, 118 ft, 80 ft, 39 ft, 20 ft, and 12 ft from the shock tube exit. To measure the pressure applied to the specimens, two gages were located on opposite sides of the tube 1.5 in. upstream of the exit. Kulite strain-gaged-diaphragm pressure transducers with a 200 psi maximum pressure range were used at all locations except at the 166-ft location, where a 5 ksi gage was used due to its proximity to the explosive charge. Data from the eight pressure gages was collected using high-resolution Genesis N7 and Nicolet Odyssey digital recording units. The Genesis was set to record at 10^7 samples/s for 500 ms, and the Nicolet at 10^6 samples/s for 1.3 s. Table 4 show the peak reflected overpressure, positive phase duration, and reflected impulse as measured at the two gages located 1.5-in. upstream of the shock tube exit.

Table 4. Measured load parameters in the large diameter shock tube.

Test	Sample	Charge Type	Peak Reflected Overpressure (psi)		Approximate Duration (ms)		Reflected Impulse (psi-ms)	
			East[1]	West[1]	East[1]	West[1]	East[1]	West[1]
40	8-ft x 8-ft brick wall (single course)	80-ft, 200 gr/ft Primacord + 2-in x 8-in Unigel packets in tapered design (35 total)	44.2	49.4	~100	~100	1573	1570
41	8-ft x 8-ft x 5-in concrete; bolted connections at sides	80-ft, 200 gr/ft Primacord + 2-in x 8-in Unigel packets in tapered design (35 total)	41.4	41.2	~100	~100	1614	1616
42	8-ft x 8-ft x 4-in concrete spandrel; supported at mid-span	80-ft, 200 gr/ft Primacord + 2-in x 8-in Unigel packets in tapered design (35 total)	47.5	46.9	~100	~100	1656	1653
43	8-ft x 8-ft clay tile roof panel; 4/12 pitch, attached outside shock tube	80-ft, 200 gr/ft Primacord + 2-in x 8-in Unigel packets in tapered design (35 total)	48.1	46.7	~65	~65	616	591

[1] Pressure gages located 1.5-in inside shock tube and against a steel wall adjacent to the test sample

In the first three tests, three high speed video (HSV) cameras were set up to capture: (1) the rear of the sample, through a mirror, to view the initial crack pattern of the sample; (2) a side view showing in-flight fragments against a white backdrop; and (3) an overview of the test with an emphasis on the soft-catch fragment collection device to check for proper operation, i.e., to ensure that no fragments passed over or around the fragment collection system. The rear-view camera was a Phantom 7.2 HSV camera set to record 432x584 pixels at 11,000 frames/s. The side-view camera was a Phantom 7.2 HSV camera set to record 800 x 600 pixels at 6,600 frames/s. The overview camera was a Phantom 7.1 HSV camera set to record 800 x 600 pixels at 4,700 frames/s. In the last test, the first camera was used to view the top surface rather than the rear surface of the clay tile roof. Other than this, the camera setup was the same as in the first three tests.

2.6 FRAGMENT COLLECTION SYSTEM

Considerable effort was invested in designing and building a soft-catch fragment collection device. Figure 9 shows the final design comprised of a 10-ft-wide by 12.5-ft-high by ~3-ft-thick wall, built from layers of fabric and cardboard, and mounted in a rigid steel structure. More specifically, the cardboard layers consisted of bundles of 4'×8'×2" honeycomb cardboard sheets. The cardboard bundles were stacked three high to achieve a height of 12 ft. The fabric layers

consisted of Kevlar sheets stapled to heavy-duty canvas tarps. The fabric layers were looped over three 4-in-thick lengths of steel tubing that extended across the top of the steel structure. Two of the square steel tubes were bolted to the steel structure. The third steel tube was placed loosely on top of the other two. A separate wall located 12.5 ft from the test sample was built for each test. The wall extended somewhat above the top and 39 in. below the bottom of the test sample.

Figure 10 shows a photograph of the test setup with the soft-capture fragment collection system on the right hand side. After each test, fragments were extracted from within the honeycomb cardboard by pulling off one side of the cardboard and emptying the contents into bins. Fragments near the fragment collection system, including those outside of the concrete pad, were also collected. However, to be included with the debris that would later be imaged and evaluated, these additional fragments had to be large enough that they clearly originated from the test specimen based on a brief visual inspection.

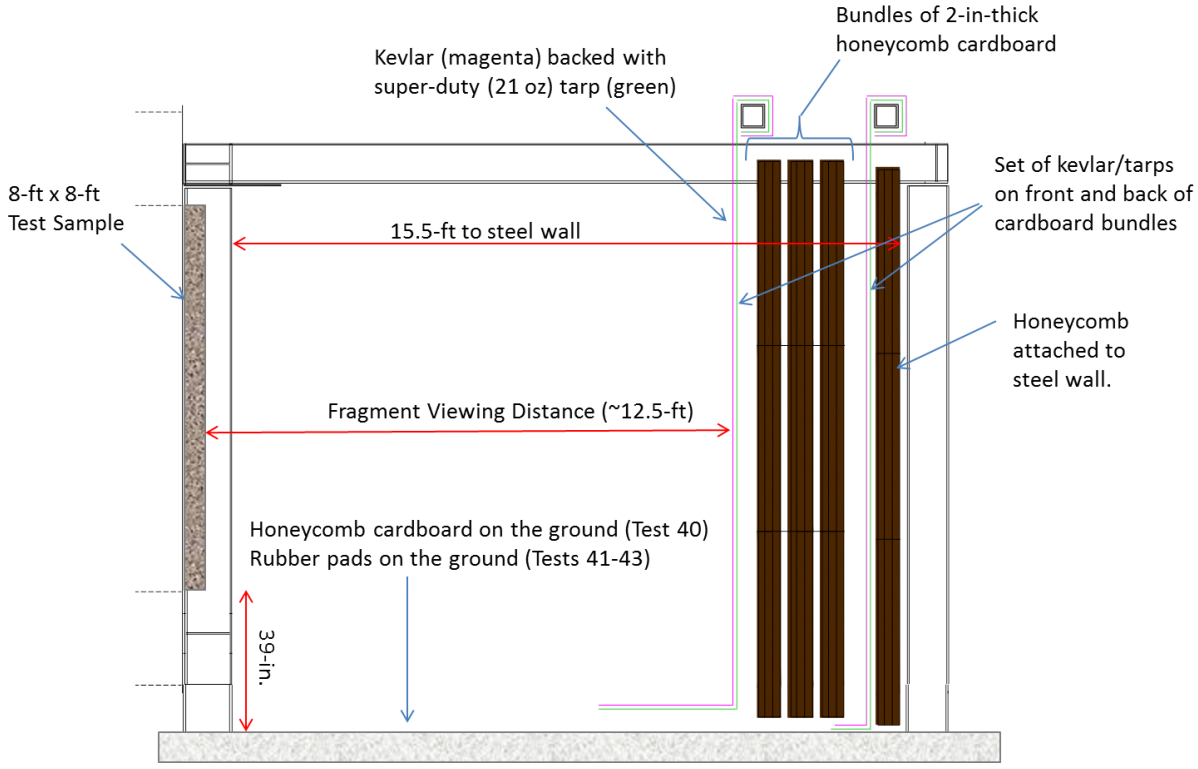

Figure 9. Design of the soft-capture fragment collection system.

Figure 10. Photograph of the soft-capture fragment collection system.

3 RESULTS OVERVIEW

3.1 BRICK WALL (TEST 40)

Figure 11 shows the reflected pressure-time history for the brick wall sample in Test 40. The overpressure spiked to 47-psi for about 2-msec, but then immediately dropped to 30-psi for about 30-msec.

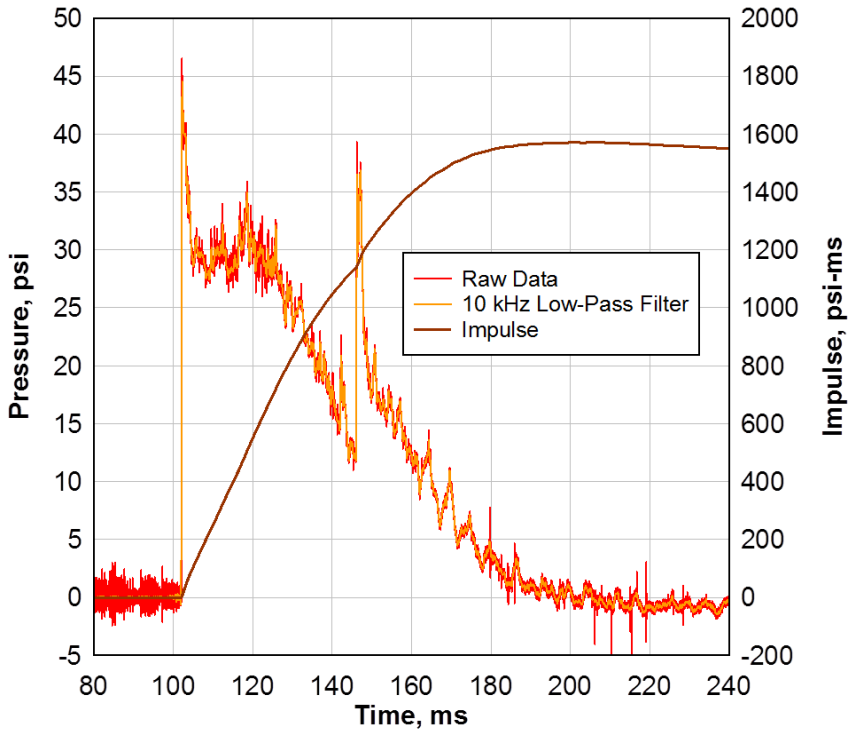

Figure 11. Reflected pressure-history for the brick wall in Test 40.

Figure 12 shows the early-time evolution of the brick wall as recorded by the rear-view HSV camera. Notice that brick fracture led to a long vertical crack, already clearly visible at 10ms. In addition, mortar joint failure led to an increasing number of horizontal and stair-stepped diagonal cracks as time progressed.

Figure 13 shows the later-time evolution of the brick wall as recorded by the overview HSV camera. Clearly, many of these fragments formed due to failures along the mortar joints. In other words, many of the fragments were individual whole bricks or clusters of whole bricks. This behavior has been observed previously in other tests; see, e.g., [9] [10] [4] [7].

Figure 12. Early-time failure of the brick wall in Test 40 as recorded by the rear-view HSV camera.

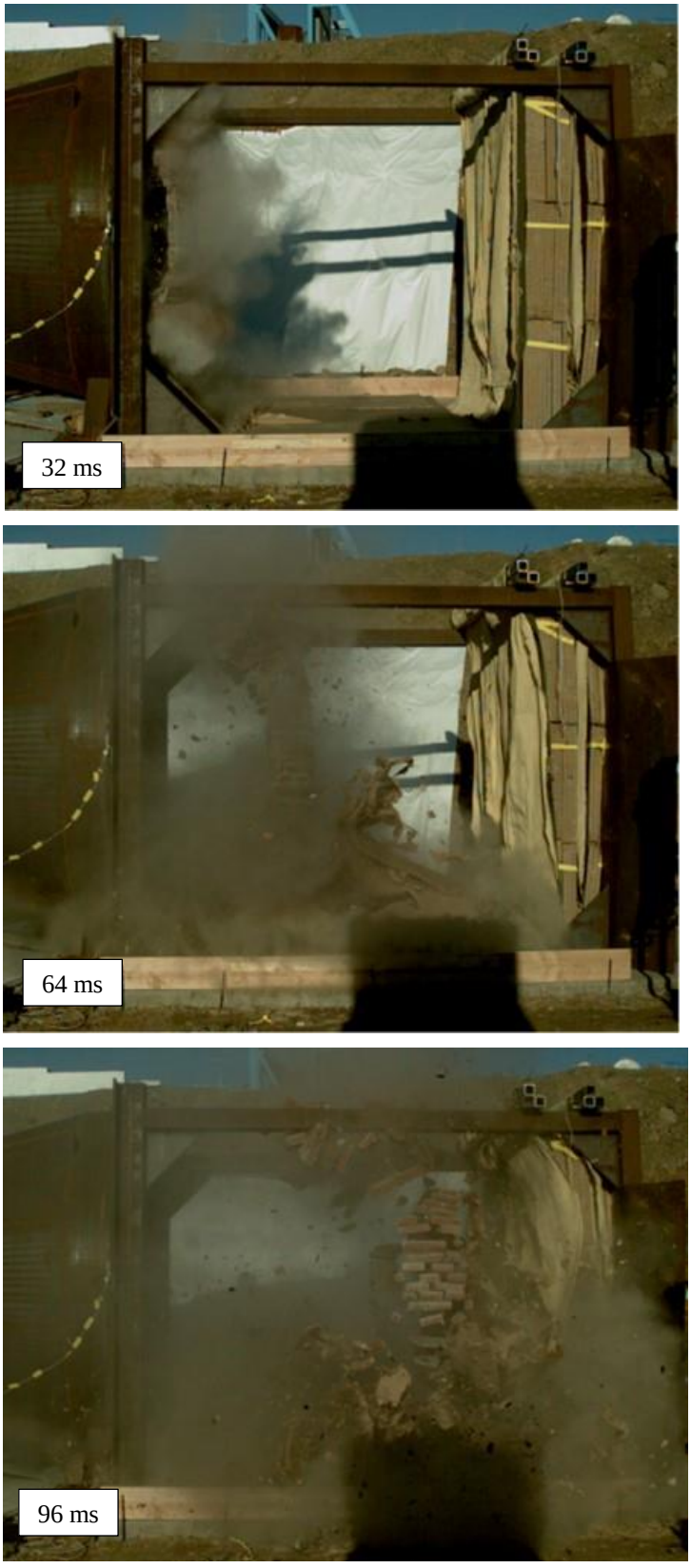

Figure 13. Later-time failure of the brick wall in Test 40 as recorded by the overview HSV camera.

3.2 STRUCTURAL CONCRETE PANEL (TEST 41)

Figure 14 shows the reflected pressure-time history of the reinforced concrete structural panel in Test 41. The overpressure spiked to 41-psi for about 2-msec, but then immediately dropped to 27-psi for about 20-msec.

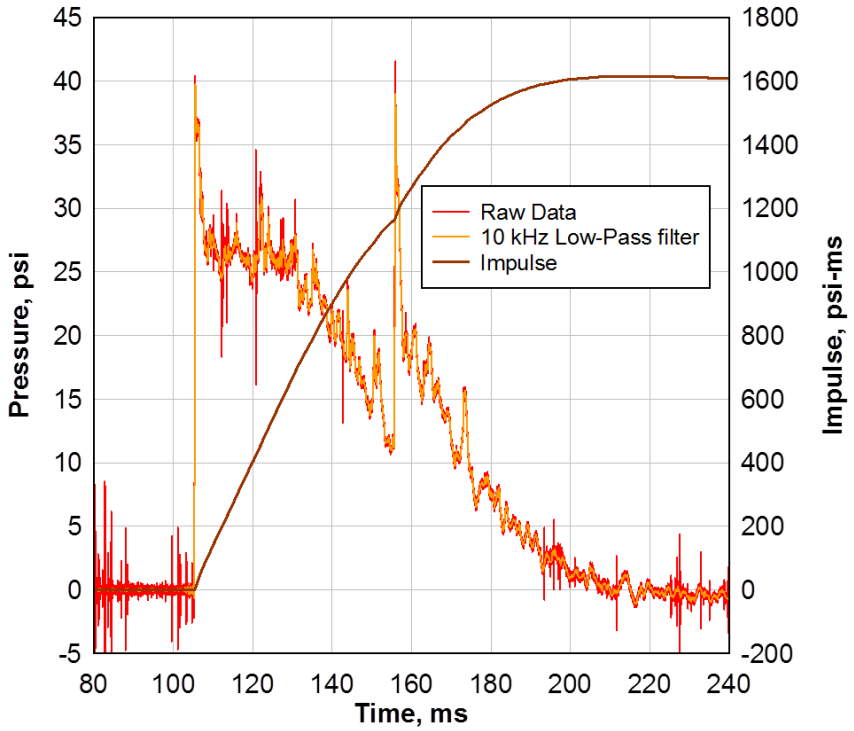

Figure 14. Reflected pressure-history for the reinforced concrete structural panel in Test 41.

Figure 15 shows the early-time evolution of the reinforced concrete structural panel as recorded by the rear-view HSV camera. Notice that the panel experienced primarily horizontal flexures and fractures. In particular, 'hinges' (horizontal cracks) formed at the upper and lower quarter points.

Figure 16 shows the later-time evolution of the reinforced concrete structural panel as recorded by the overview HSV camera. While obscured by dust, these frame captures show that the top and bottom quarters of the panel continued to fracture, while the middle half of the panel remained mostly intact due to the steel reinforcing bars. Eventually, the reinforcing bars detached from the deteriorating quarter panels and the middle portion of the panel displaced downstream as a unit.

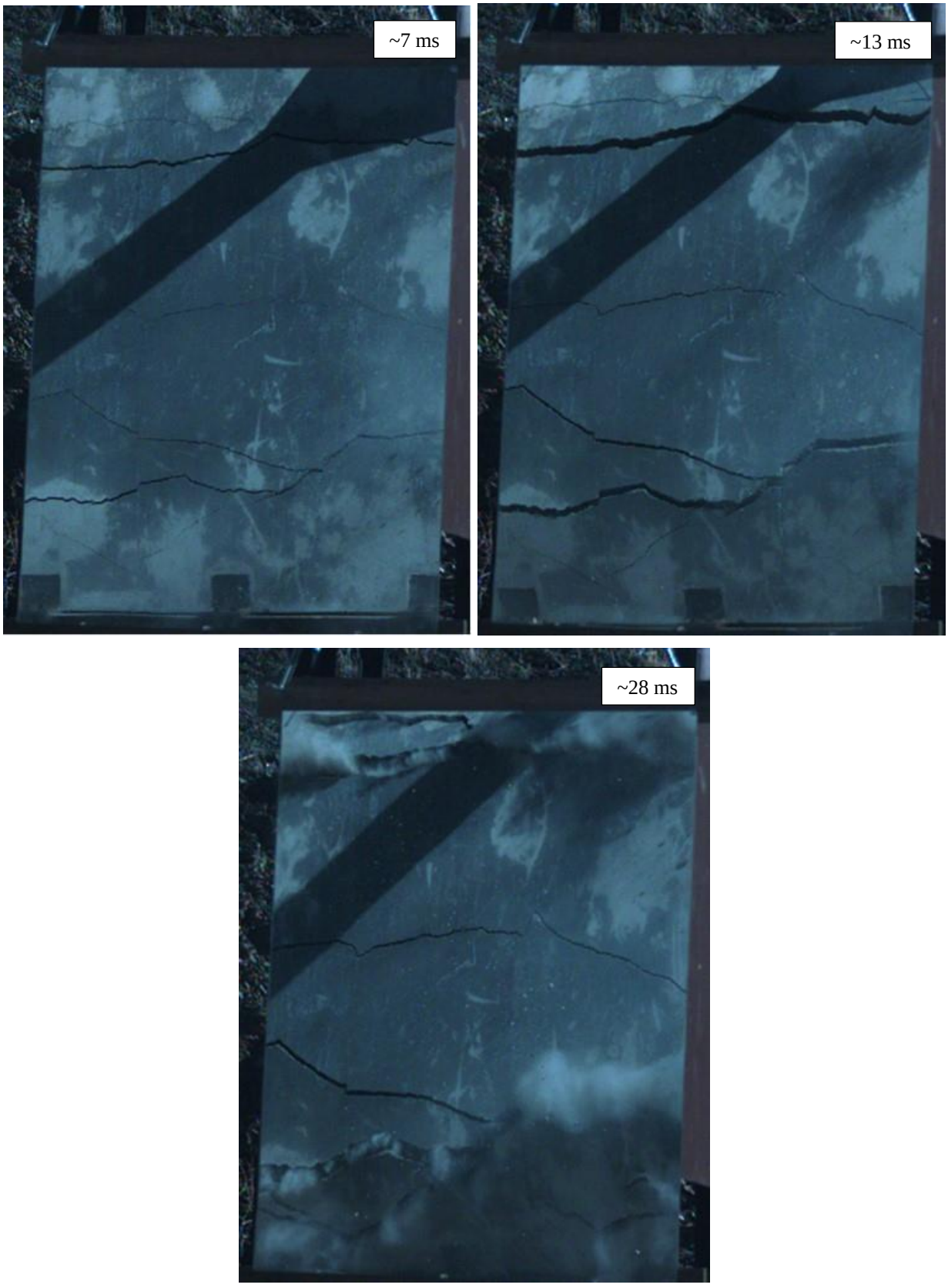

Figure 15. Early-time failure of the concrete structural panel in Test 41 as recorded by the rear-view HSV camera.

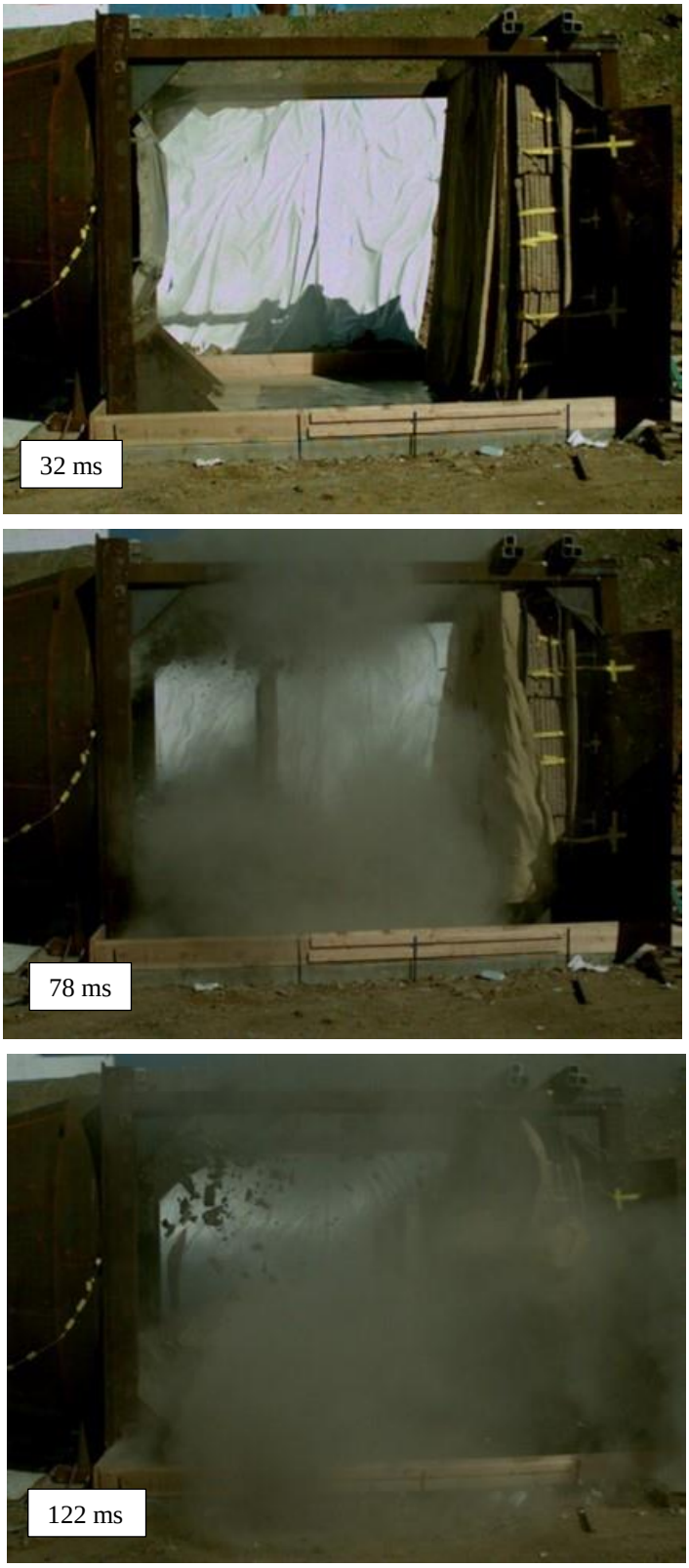

Figure 16. Later-time failure of the concrete structural panel in Test 41 as recorded by the overview HSV camera.

3.3 CONCRETE SPANDREL PANEL (TEST 42)

Figure 17 shows the reflected pressure-time history for the reinforced concrete spandrel panel in Test 42. The overpressure spiked to 47-psi for about 2-msec, but then immediately dropped to 30-psi for about 20-msec.

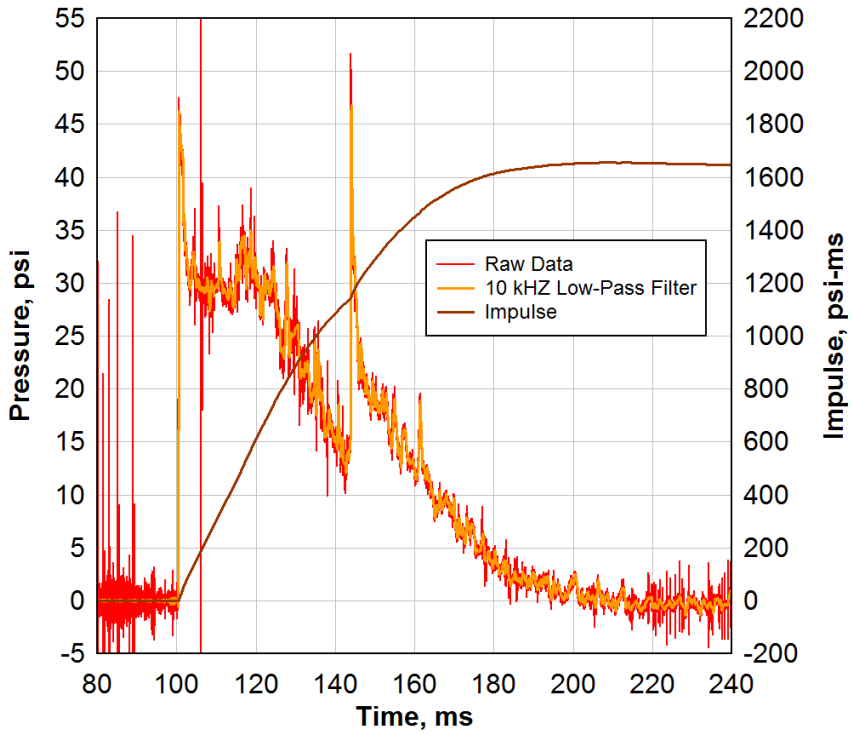

Figure 17. Reflected pressure-history for the reinforced concrete spandrel panel in Test 42.

Figure 18 shows the early-time evolution of the fracture pattern on the rear surface of the thin concrete spandrel panel as recorded by the rear-view HSV camera. As in the previous test, 'hinges' (horizontal cracks) formed near the quarter points.

Figure 19 shows the later-time evolution of the reinforced concrete spandrel panel as recorded by the overview HSV camera. While not clear from these photographs, the top and bottom quarters of the panel remained mostly intact. However, the middle half of the panel flexed, partially wrapped around the supporting HSS spandrel beam, and then eventually broke into a large number of small fragments. By contrast, in the previous test, the center of the concrete panel remained intact and the top and bottom quarters broke into fragments.

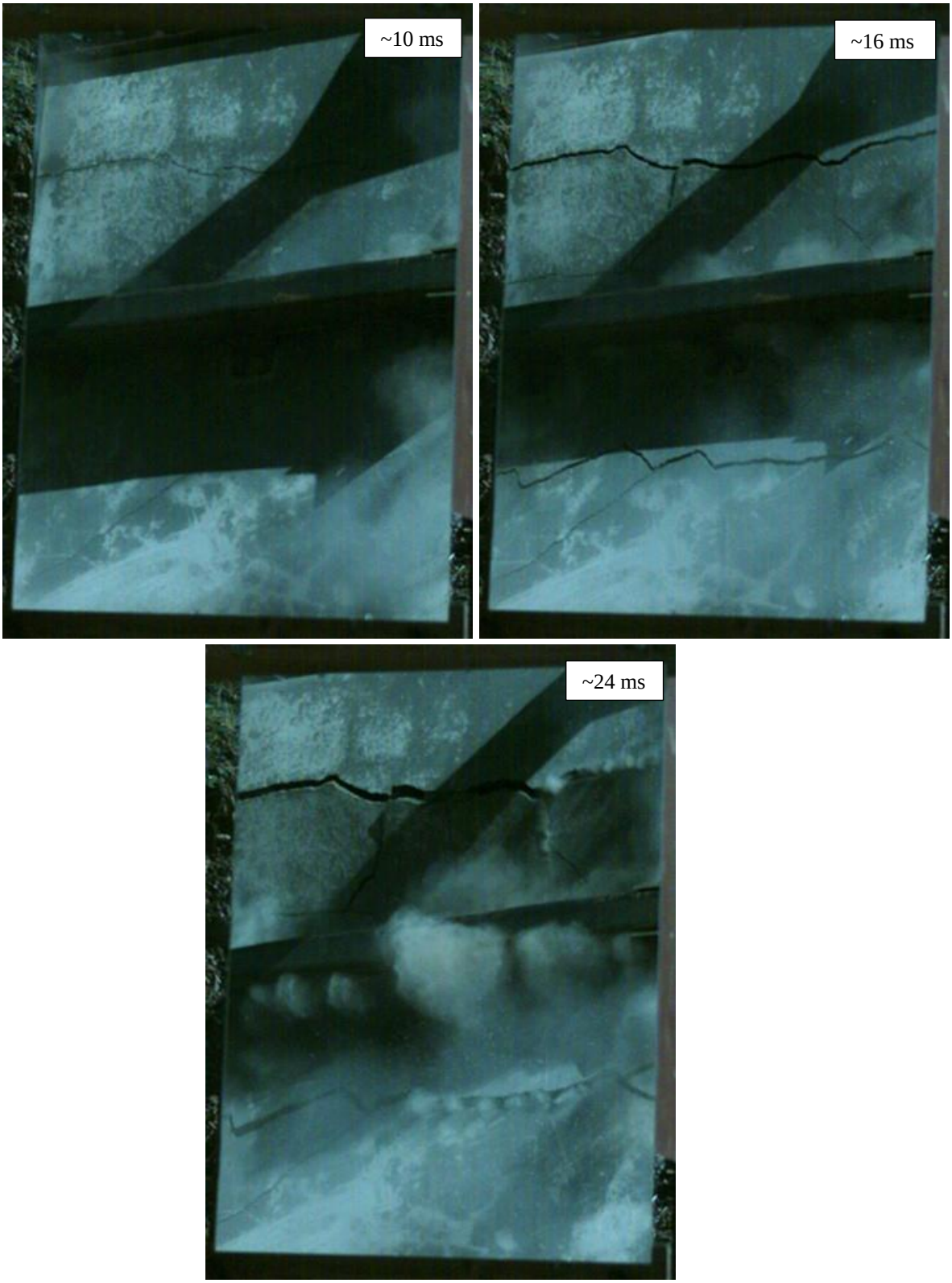

Figure 18. Early-time failure of the concrete spandrel panel in Test 42 as recorded by the rear-view HSV camera.

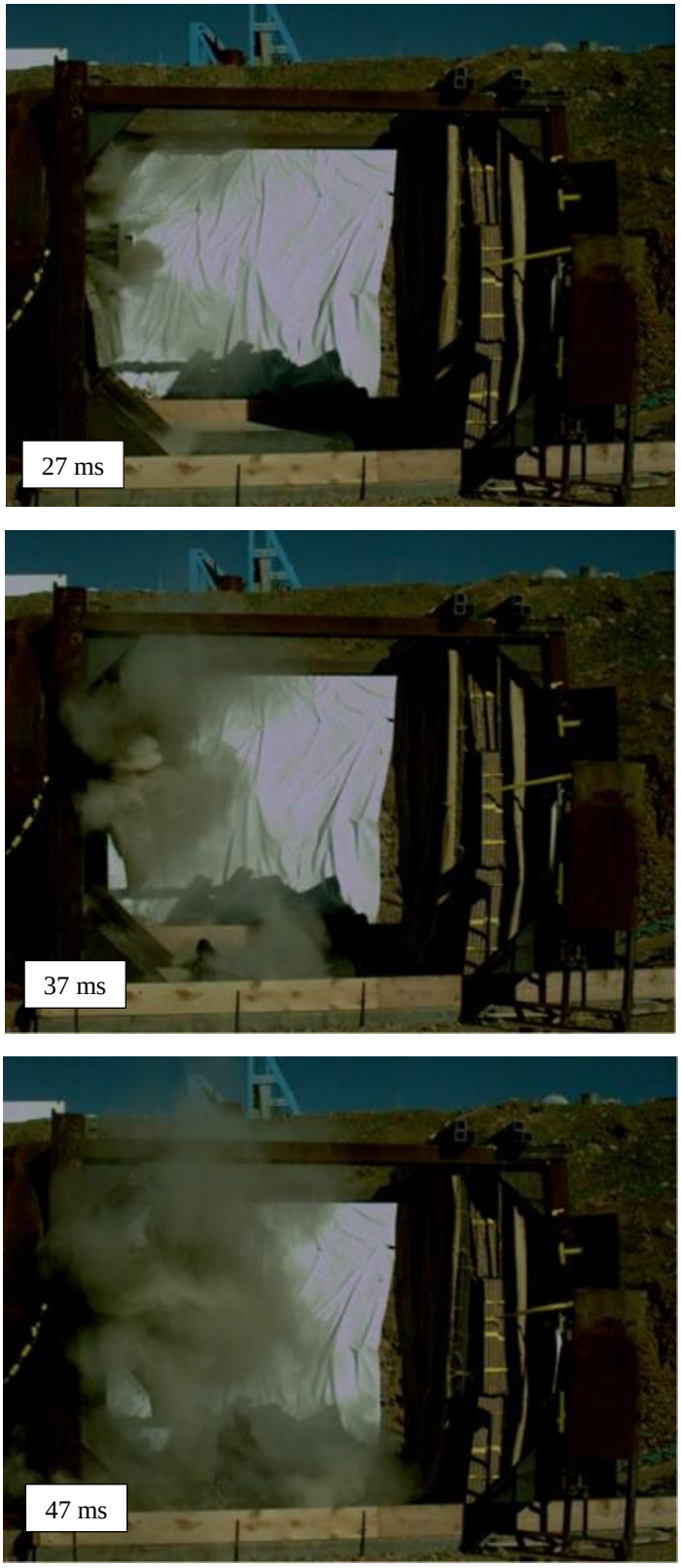

Figure 19. Later-time failure of the concrete spandrel panel in Test 42 as recorded by the overview HSV camera.

3.4 CLAY TILE ROOF (TEST 43)

Figure 20 shows the reflected pressure-time history for the clay tile roof in Test 43. The overpressure spiked to 47-psi for about 2-msec, but then immediately dropped to 15-psi for about 7-msec. The reflected peak overpressure and duration are less than in the other three tests because the clay roof only partially blocked the shock tube exit.

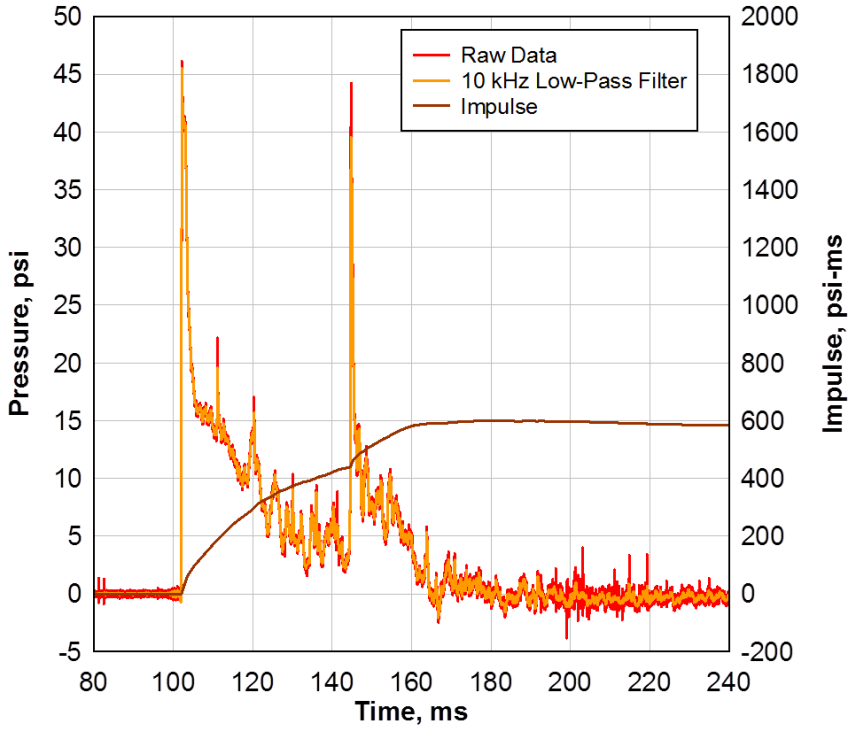

Figure 20. Reflected pressure-history for the clay tile roof in Test 43.

Figure 21 shows the early-time evolution of damage to the clay tile roof as recorded by the side-view HSV camera. While it is not apparent in these photographs, the underlayment (horizontally-spanning OSB) failed due flexure after a number of tiles had broken free.

Figure 22 shows the later-time evolution of the clay tile roof as recorded by the overview HSV camera. As time progressed, dynamic pressure progressively lifted fractured roof tiles and displaced them downstream at high velocities

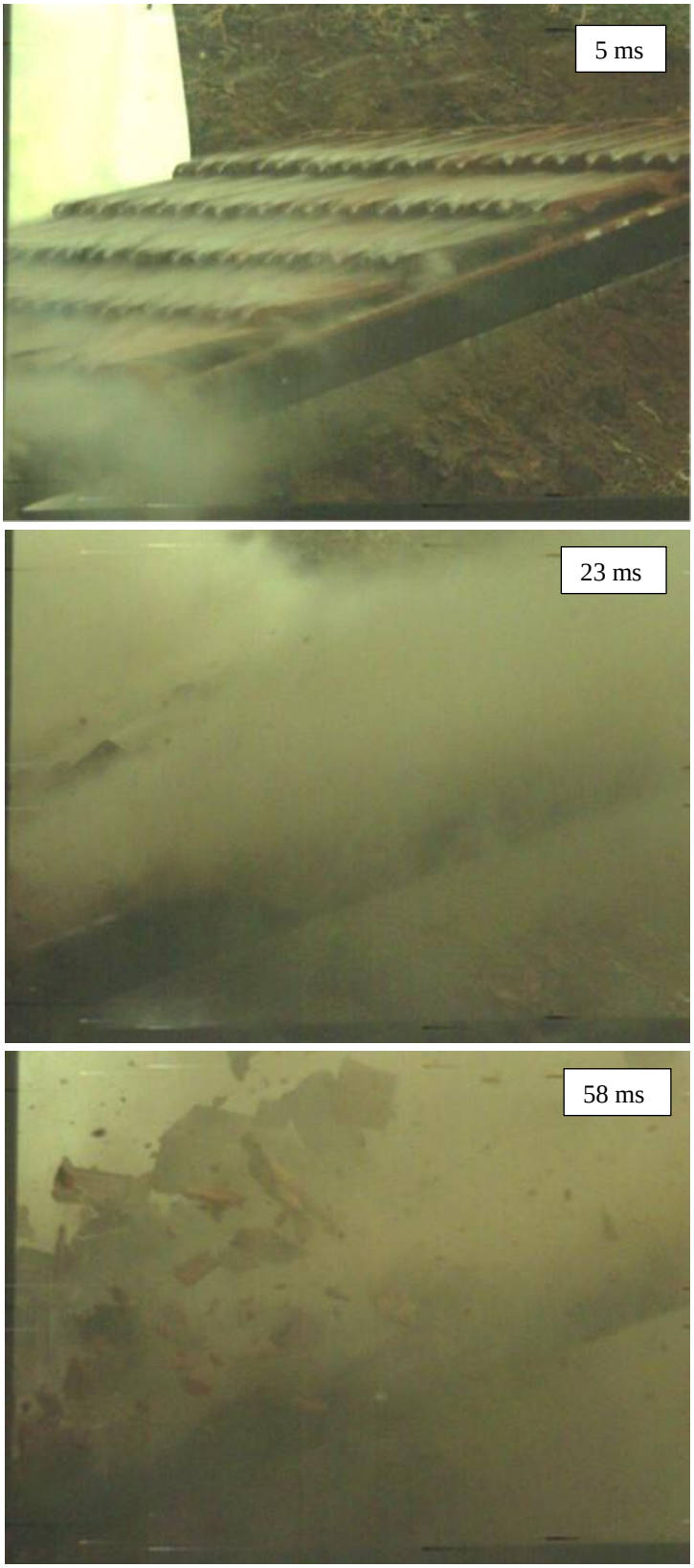

Figure 21. Early-time failure of the clay tile roof in Test 43 as recorded by the side-view HSV camera.

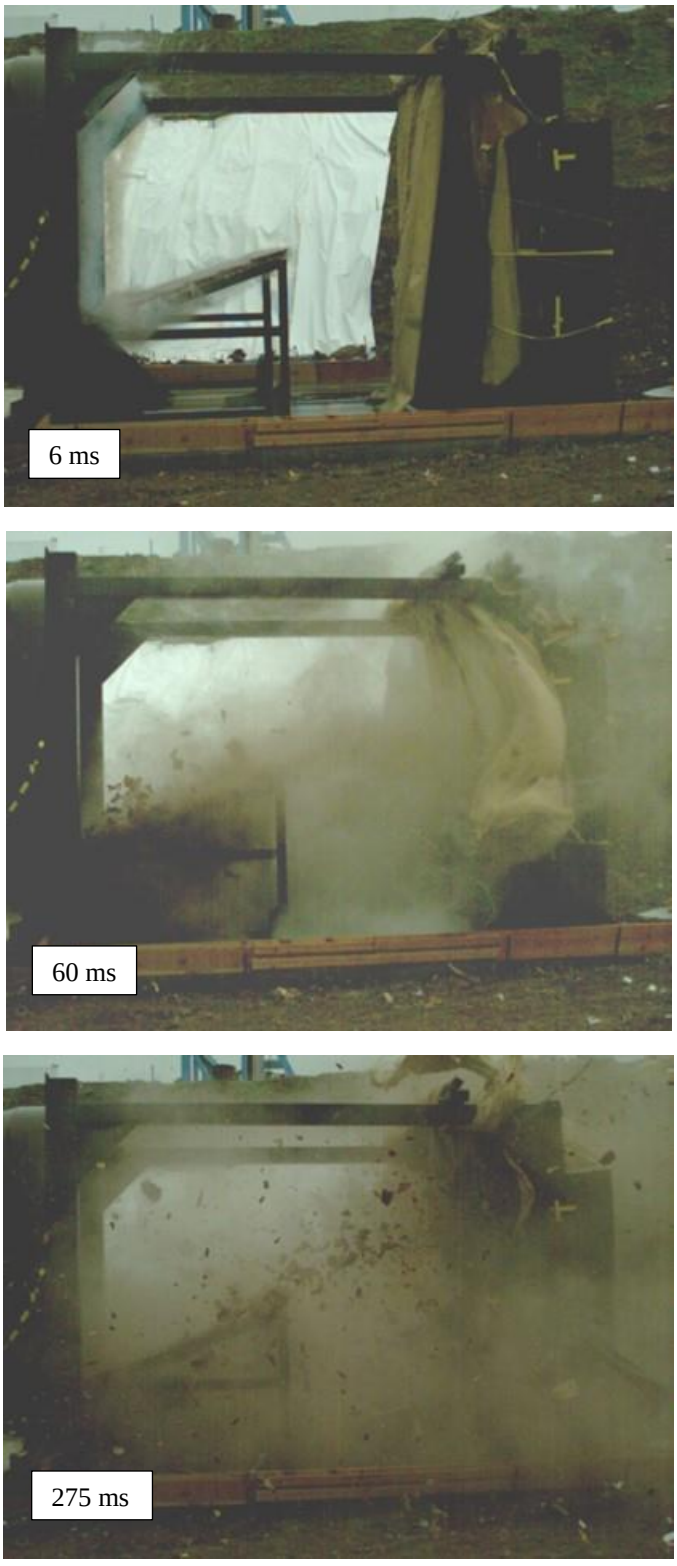

Figure 22. Later-time failure of the clay tile roof in Test 43 as recorded by the overview HSV camera.

As seen in Figure 23, the clay tiles experienced predominantly two-dimensional fragmentation, i.e., most of the larger fragments retained smooth surfaces from the upper and/or lower surface of the original tile. In the other three tests in this series, the test samples experienced predominantly three-dimensional fragmentation, i.e., most fragments were rough on all sides.

Figure 23. Photographs of clay tile roof fragments produced in Test 43.

4 ANALYSIS TECHNIQUES

4.1 SIFTING AND SAMPLING

Unlike previous test series, no attempt was made to characterize the fragment properties based on the high-speed video. Instead, the fragment masses were characterized entirely based on physical collection. Fragments weighing more than 680 grams (~1.5 lbs) were individually hand-weighed. Fragments weighing less than 680 grams were passed through a series of increasingly finer sieves to separate them into size bins; see Figure 24. Because of the very large number of fragments weighing less than 680 grams, it was impractical to characterize them all, given the limited time and budget. Instead, two random samples, each 5% of the total bin weight, were selected from each size bin. If the results of the two random samples agreed, which was approximately true in all cases, they were combined to form a single 10% random sample.

Figure 24. Fragments generated in the test series sorted into size bins through sieving.

4.2 IMAGE ANALYSIS

For each 5% sample, the fragments were manually laid out on a flat surface, being careful to separate them to avoid clusters that might appear to be a single fragment. A minimum fragment size of 0.005g was imposed because it was impractical to manually separate fragments smaller than that. The resulting display was photographed and analyzed using SigmaScan Pro, a well-known commercial image analysis software package. To improve fragment characterization, SigmaScan Pro was used to convert the color images to high-contrast grayscale images. The resulting SigmaScan Pro images were inspected and lines were drawn manually between adjacent fragments as necessary to ensure that each fragment was counted individually. While this required extra effort, it eliminated the need to use special logic functions and VBA code, as described in Reference [1], to enforce the 0.005g lower limit. Starting from the high-contrast digital images, SigmaScan Pro was used to estimate the in-plane dimensions, cross-sectional areas, and other geometrical information for each fragment. As an example, Figure 25 shows the original and processed image for a 5% sample taken from Sieve No. 4 in Test 43.

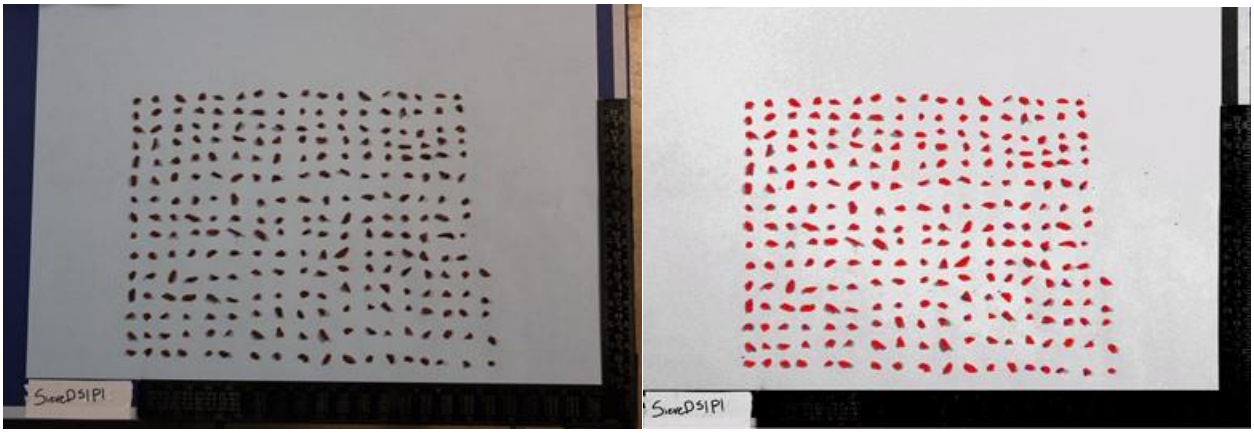

(a) Original full-color photograph (b.) High-contrast digital image produced by SigmaScan Pro.

Figure 25. Fragments captured by Sieve no. 4 in Test 43.

The SigmaScan Pro results for two-dimensional in-plane fragment dimensions and cross-sectional fragment areas were used to estimate three-dimensional fragment masses. More specifically, for thin enough samples and large enough fragments, fragments inherit two smooth surfaces from the original sample. Then:

$$M_i = \rho t A_i$$

where M_i is the mass of fragment i, A_i is the cross-sectional area of fragment i as measured by SigmaScan Pro, ρ is the density, and t is the original sample thickness, e.g., $t = 0.25$ inches for the plate glass tests. For thicker samples and smaller fragments, the fragments will be rough on all sides, i.e., they will not inherit any smooth surfaces from the original sample. Then:

$$M_i \approx A_i \cdot \frac{\sum M_j}{\sum A_j}$$

where the sums refer to all of the fragments in a given size bin. In other words, the mass-to-area ratio of any individual fragment is assumed to be approximately equal to the cumulative mass to cumulative area ratio of all fragments in the same bin.

4.3 CURVE FITTING

Microsoft Excel was used to fit power law and Weibull size distributions to the experimental fragment masses. To define power law and Weibull size distributions, it is first necessary to define complementary cumulative distribution functions (CDFs) and probability density functions (PDFs). The complementary *cumulative distribution function* $F(M)$ is the number fraction of fragments with masses greater than or equal to *M*. Similarly, the *probability density function* $f(M)$ is the number fraction of fragments with masses in a range *dM* centered on *M* divided by *dM*.

Notice that $F(x)$ is monotone decreasing such that $F(0)=1$ and $F(\infty)=0$. In addition, notice that $f(x)$ is always non-negative such that:

$$\int_0^\infty f(x)dx = 1.$$

Finally notice that:

$$F(M) = -\int_M^\infty f(x)dx; \;\; f(M) = -\frac{dF}{dM}.$$

These definitions assume an infinite range of fragment sizes. However, experimental results always obtain a limited finite range of fragment sizes. The CDFs and PDFs over a limited range $M_{\min} \le M \le M_{\max}$ are related to the CDFs and PDFs over an infinite range as follows:

$$\tilde{F}(M) = \frac{F(x) - F(M_{\min})}{F(M_{\max}) - F(M_{\min})}$$

$$\tilde{f}(M) = \frac{f(M)}{F(M_{\max}) - F(M_{\min})}.$$

The *count mean mass* is defined as follows:

$$M_{avg} = \int_0^\infty Mf(M)dM$$

for an infinite range and:

$$\tilde{M}_{avg} = \int_{M_{\min}}^{M_{\max}} M\tilde{f}(M)dM = \frac{\int_{M_{\min}}^{M_{\max}} Mf(M)dM}{\int_{M_{\min}}^{M_{\max}} f(M)dM}$$

for a finite range.

Normalizing by the count mean mass, *Weibull size distributions* may be defined as follows:

$$F(M) = \exp\left[-c\left(\frac{M}{M_{avg}}\right)^r\right]$$

$$f(M) = \frac{c\,|r|}{M_{avg}}\left(\frac{M}{M_{avg}}\right)^{r-1}\exp\left[-c\left(\frac{M}{M_{avg}}\right)^r\right]$$

where r is a free parameter and where:

$$c = \Gamma\left(1+\frac{1}{r}\right)^r .$$

Similarly, power law size distributions may be defined as follows:

$$F(M) = \begin{cases} 1-(M/M_{\max})^r & r>0 \\ (M/M_{\min})^r & r<0 \end{cases}$$

$$f(M) = \begin{cases} \dfrac{r}{M_{\max}}\left(\dfrac{M}{M_{\max}}\right)^{r-1} & r>0 \\ \dfrac{|r|}{M_{\min}}\left(\dfrac{M}{M_{\min}}\right)^{r-1} & r<0 \end{cases} .$$

Notice that Weibull size distributions are approximately equal to power law size distributions for sufficiently large or small fragments, depending on the sign of r.

The initial curve fitting procedure used fixed bin widths. However, this resulted in overpopulated small bins, underpopulated large bins, and suboptimal fits overall. We thus used variable bin widths that minimized bin-to-bin variations in mass.

To further examine the effects of binning, three types of fits were considered: a coarse fit based on 10 sizes bins; a medium fit based on 35 size bins; and a fine fit based on 150 size bins. The medium fit tended to obtain the best results and was thus used in all cases reported here.

The rear-view and side-view HSV camera data tended to obtain a relatively narrow range of fragments, often only one or two orders-of-magnitude, which affected the perceived average

fragment size. The average fragment size was thus based on the physically-collected data in all cases. For additional information on the curve fitting procedures used here see, e.g., Table 7 in Reference [1]

As an example, Figure 26 shows fragment mass PDFs for the two random 5% subsets taken in Test 42. In this test, and in the other three tests, the two random 5% samples were in good agreement with each other. All subsequent results are show combinations of the two 5% samples.

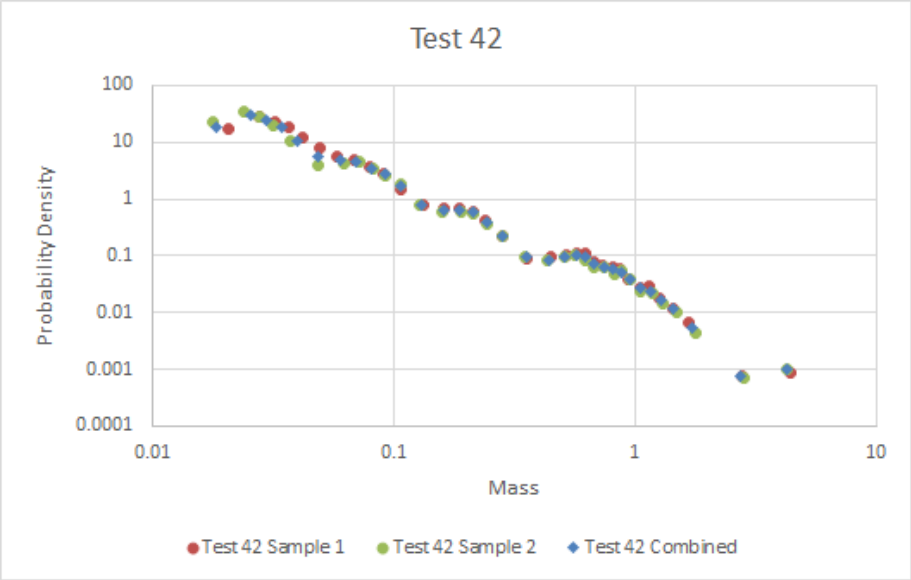

Figure 26. The mass PDFs in Test 42 based on two random 5% subsets of fragments less than 680g.

5 TEST RESULTS

Table 5 and Table 6 summarize the physical collection results. For completeness, these tables include two results from the second test series [2]. In Table 6, green shading indicates an acceptable fit while white shading indicates an unacceptable fit. In all cases, the acceptable fits involved power laws rather than Weibull size distributions.

Table 5. Statistical parameters for physically-collected fragment mass distributions.

Test	Test Sample	Material Thickness	Material Strength (psi)	Peak Overpressure (psi)	# Frags Observed	Mass Frags Observed (g)
20 [2]	CMU Wall	7.625"[1]	2,000[2]	73	811,283	993,725.7
40	Brick Wall	3.265"	8,640[2]	47	5,340	2,810
21 [2]	Concrete Panel	5.5"	6,940[3]	48	~0	~0
41	Concrete Panel	5"	4,000	41	31,808	7,147
42	Concrete Panel	4"	4,000	47	44,374	7,814
43	Clay Tile Roof		7,940[2]	47	5,610	9,704

(1.) CMUs ("cinder blocks") are hollow, open at the top and bottom, with nominal sidewall thicknesses of 1.25-in. and centerwall thicknesses of 1-in. (2.) Individual blocks, bricks, or tiles. (3.) The high strength of the concrete prevented this test sample from experiencing substantial fragmentation. A moderate number of small, slow fragments were observed in high-speed video but only a few of these reached the soft-catch fragment collection device.

Table 6. Best-fit Weibull and power law parameters based on physically-collected fragment mass data

Test	Test Sample	Fitting Parameters Method 2 – Jul 2018					Fitting Parameters Method 3 – September 2018				
		Weibull r	Power r	M_{min} (g)	M_{max} (g)	$\widetilde{M}_{avg}$ (g)	Weibull r	Power r	M_{min} (g)	M_{max} (g)	$\widetilde{M}_{avg}$ (g)
20	CMU Wall	0.63	–1.00	0.2	7	0.160	0.26	–1.02	0.01	1,500	0.610
40	Brick Wall	0.53	–0.81	0.017	7	0.265	0.38	–0.81	0.007	43	0.413
41	Concrete Panel	0.57	–1.05	0.025	7	0.173	0.37	–0.95	0.004	135	0.225
42	Concrete Panel	0.57	–1.07	0.025	7	0.134	0.39	–1.04	0.01	93	0.176
43	Clay Tile Roof	0.45	–0.80	0.006	10	0.191	0.22	–0.83	0.006	136	0.412

This effort compared three different automated fitting methods, which varied in terms of how the bin limits, the maximum fragment sizes, and so forth were chosen. For all three methods, for Weibull distributions, a $\chi 2$ approach was used to generate a single best fit for both PDFs and CDFs. In addition, for power law distributions, CDFs were fit first using $\chi 2$, then PDFs were fit.

Table 6 shows the results only for Methods 2 and 3. The main difference is that Method 2 uses relatively small maximum fragment sizes while Method 3 uses relatively large maximum fragment sizes. As seen in Table 6, changing the maximum fragment size has a major effect on the best-fit Weibull parameters but only a minor effect on the best-fit power law parameters.

Figure 27 and Figure 28 show the best-fit Weibull and power law size distributions, respectively, obtained using Method 3 for the brick wall in Test 40. Figure 29 and Figure 30 show the best-fit Weibull and power law size distributions, respectively, obtained using Method 3 for the reinforced concrete structural panel in Test 41. Figure 31 and Figure 32 show the best-fit Weibull and power law size distributions, respectively, obtained using Method 3 for the reinforced concrete spandrel panel in Test 42. While the reinforced concrete panels used in Tests 41 and 42 were significantly different, Figure 33 shows that they obtained essentially the same fragment size distribution. Figure 34 and Figure 35 show the best-fit Weibull and power law size distributions, respectively, obtained using Method 3 for the clay tile roof in Test 43. For comparison, Figure 36 and Figure 37 show the best-fit Weibull and power law size distributions, respectively, obtained using Method 2 for the clay tile roof in Test 43. In this case, eliminating the largest fragments leads to substantially better fits. The largest fragments from the clay tile roof were highly irregular, because they formed at significantly different times and under significantly different conditions. Simple fitting functions are not always able to adequately represent highly-diverse fragment populations.

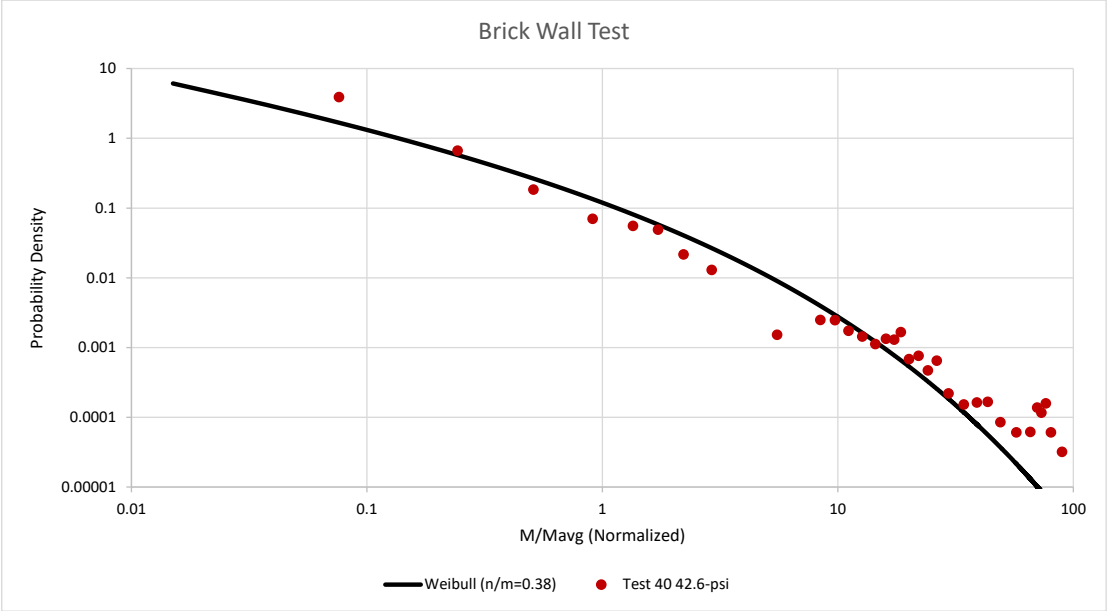

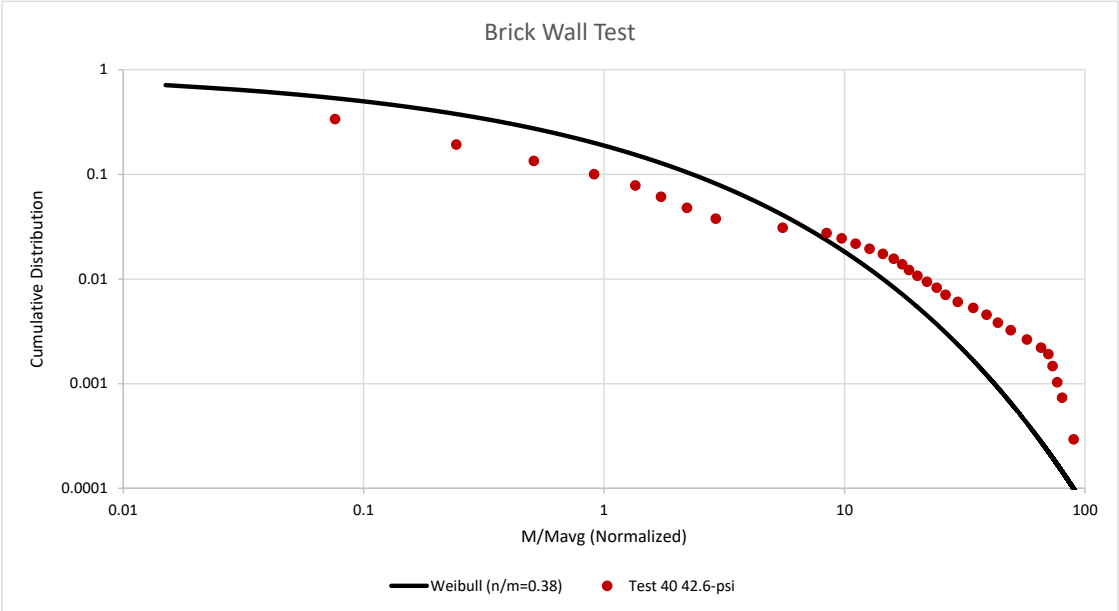

Figure 27. Best-fit Weibull mass distribution for physically-collected test data for PDF (top) and CDF (bottom) for Test 40 involving brick.

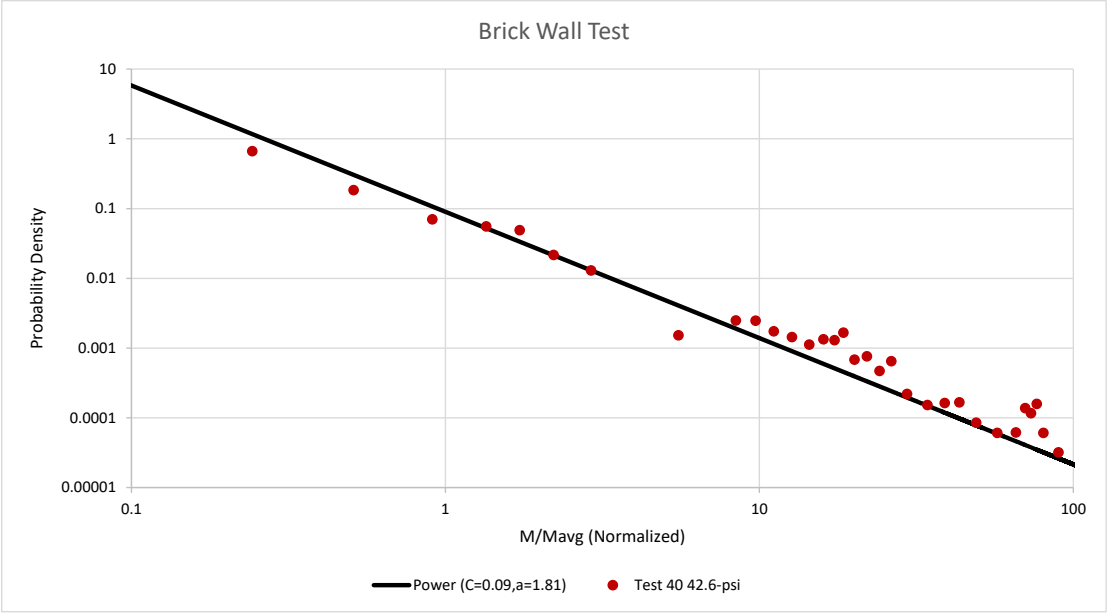

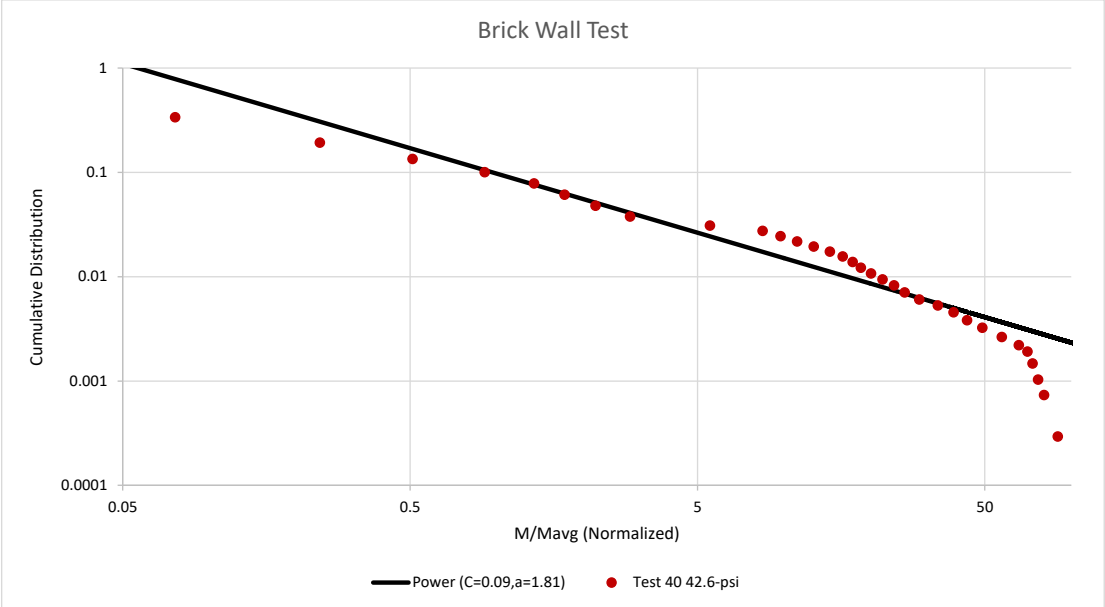

Figure 28. Best-fit power law mass distribution for physically-collected test data for PDF (top) and CDF (bottom) for Test 40 involving brick.

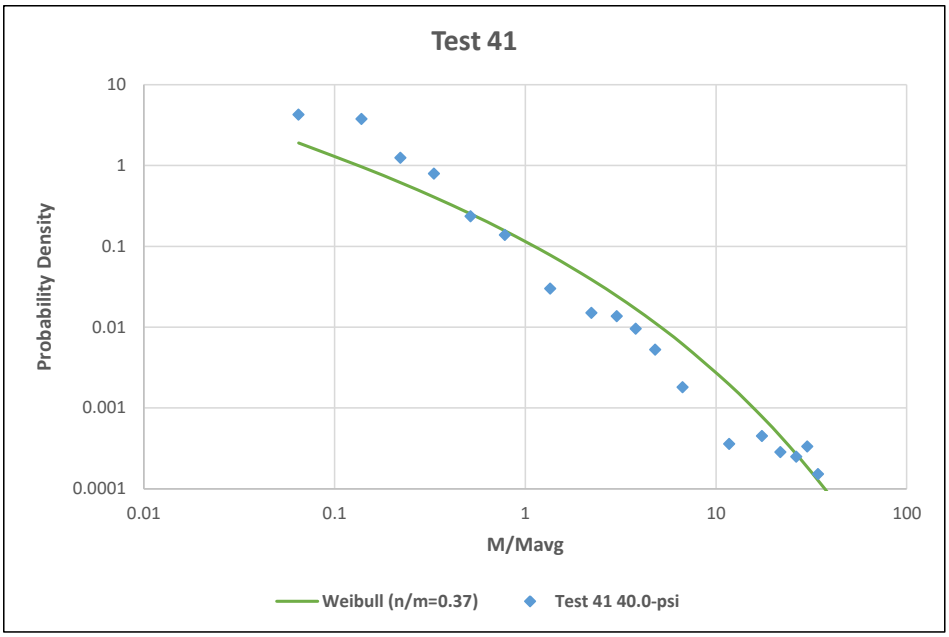

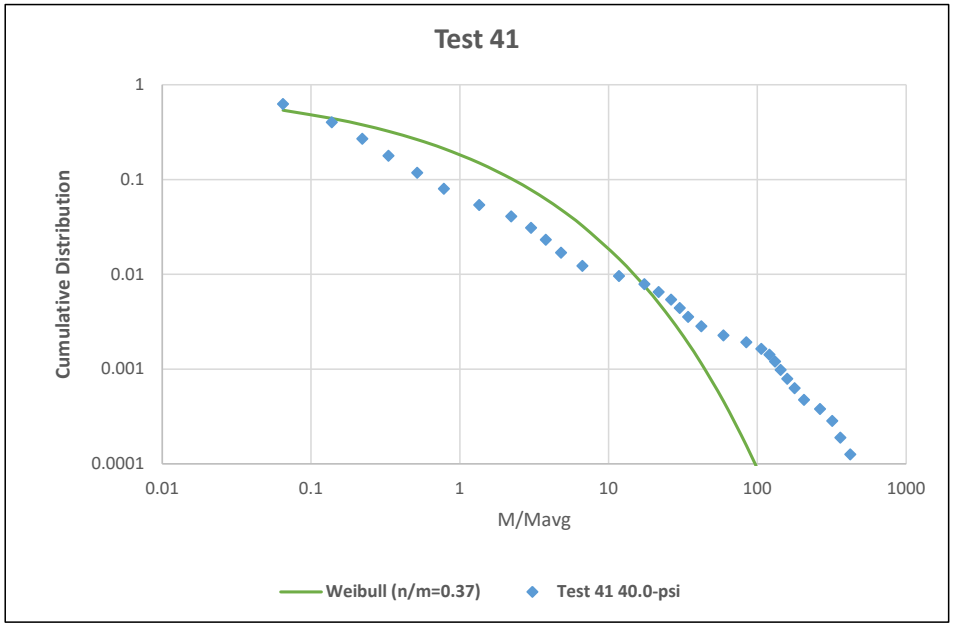

Figure 29. Best-fit Weibull mass distribution for physically-collected test data for PDF (top) and CDF (bottom) for Test 41 involving concrete.

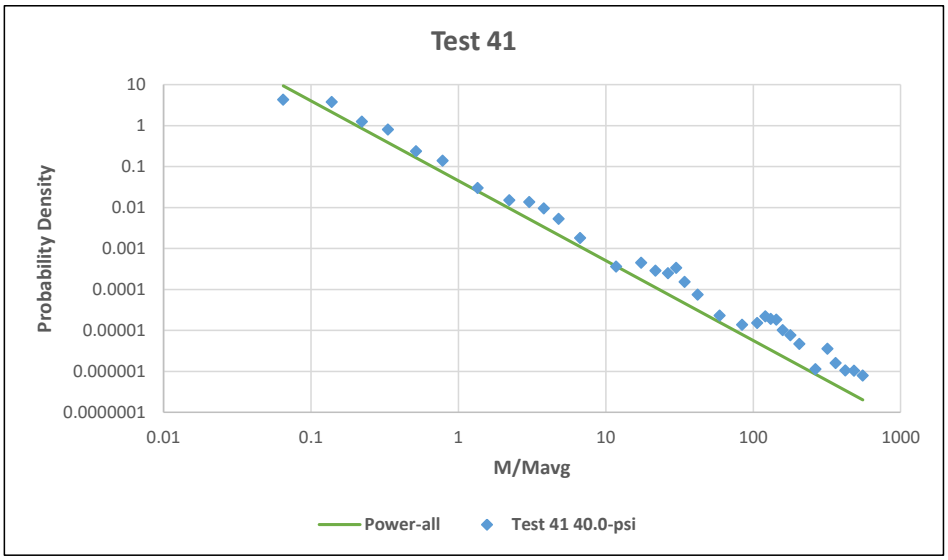

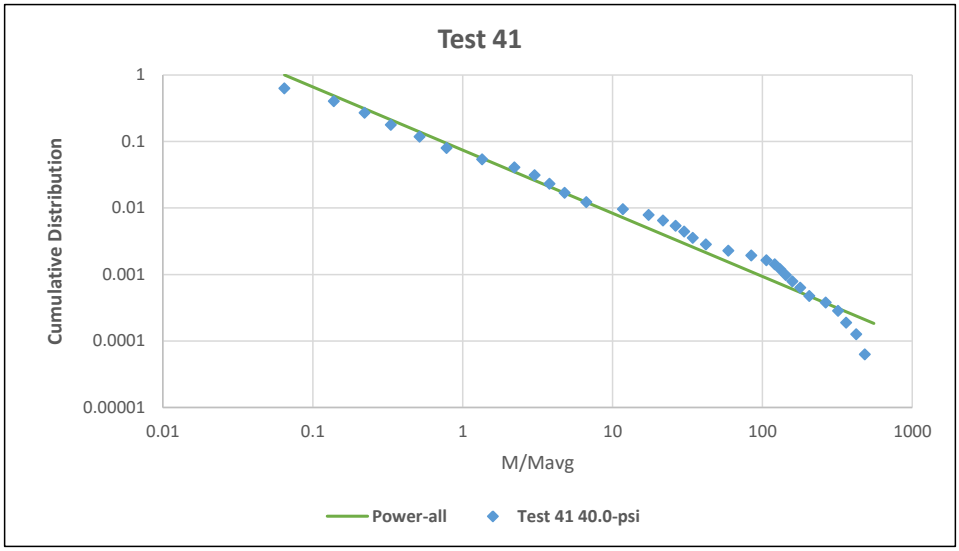

Figure 30. Best-fit power law mass distribution for physically-collected test data for PDF (top) and CDF (bottom) for Test 41 involving concrete.

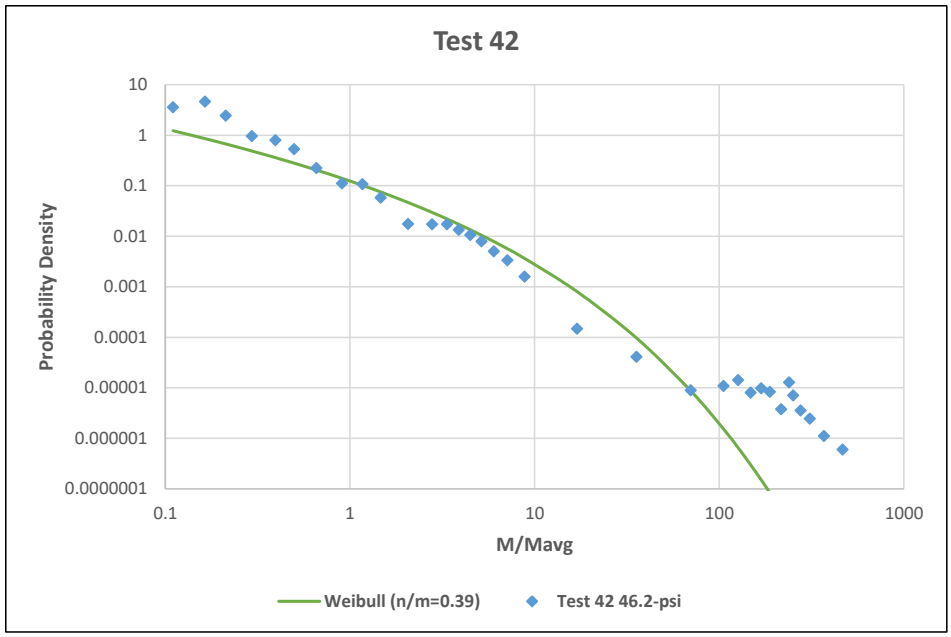

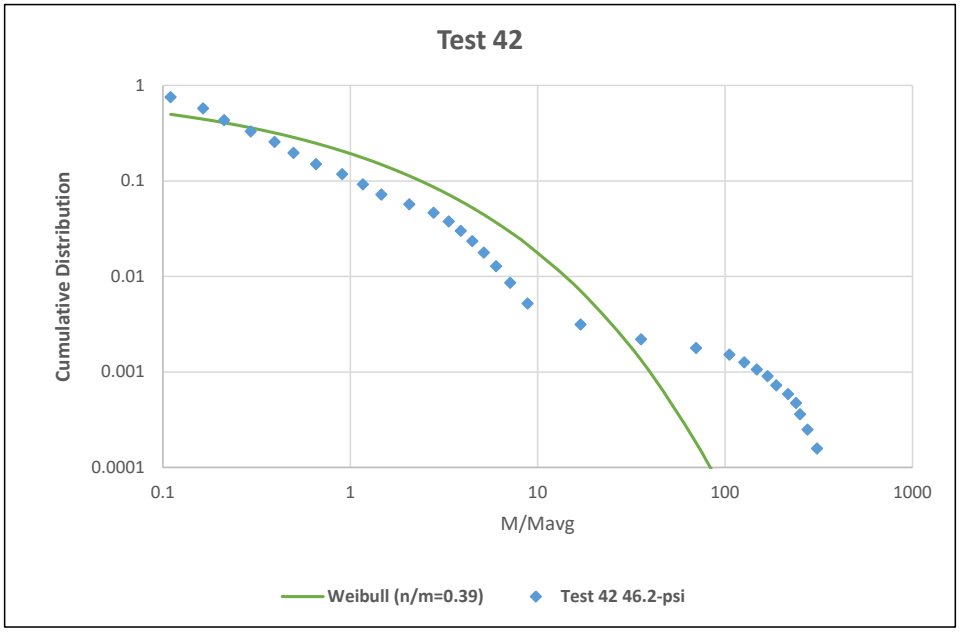

Figure 31. Best-fit Weibull mass distribution for physically-collected test data for PDF (top) and CDF (bottom) for Test 42 involving concrete.

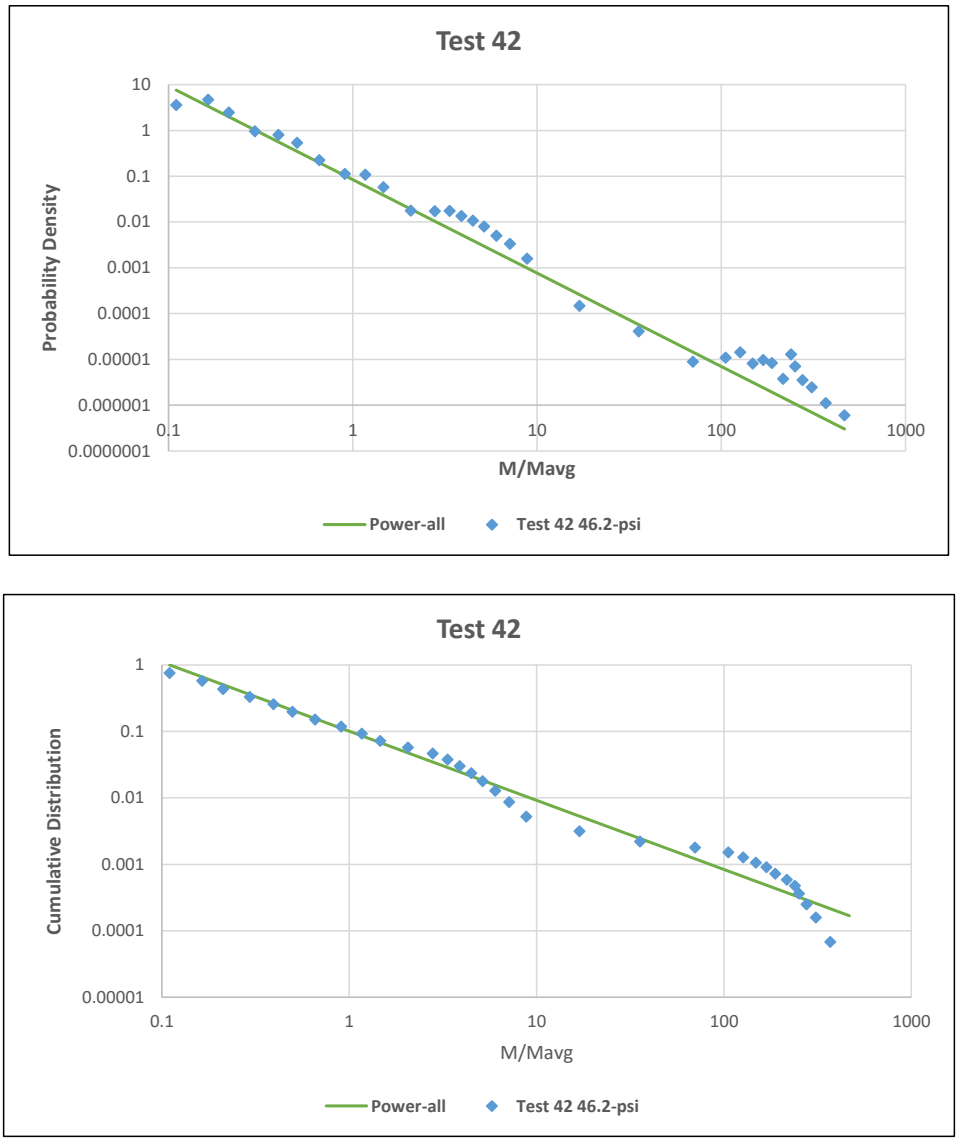

Figure 32. Best-fit power law mass distribution for physically-collected test data for PDF (top) and CDF (bottom) for Test 42 involving concrete.

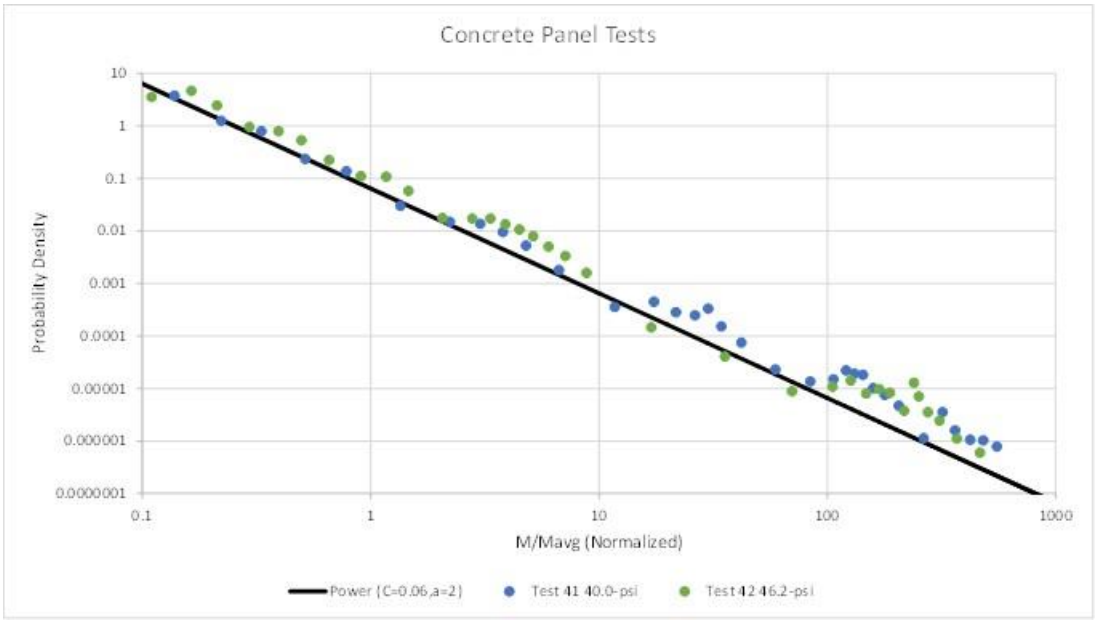

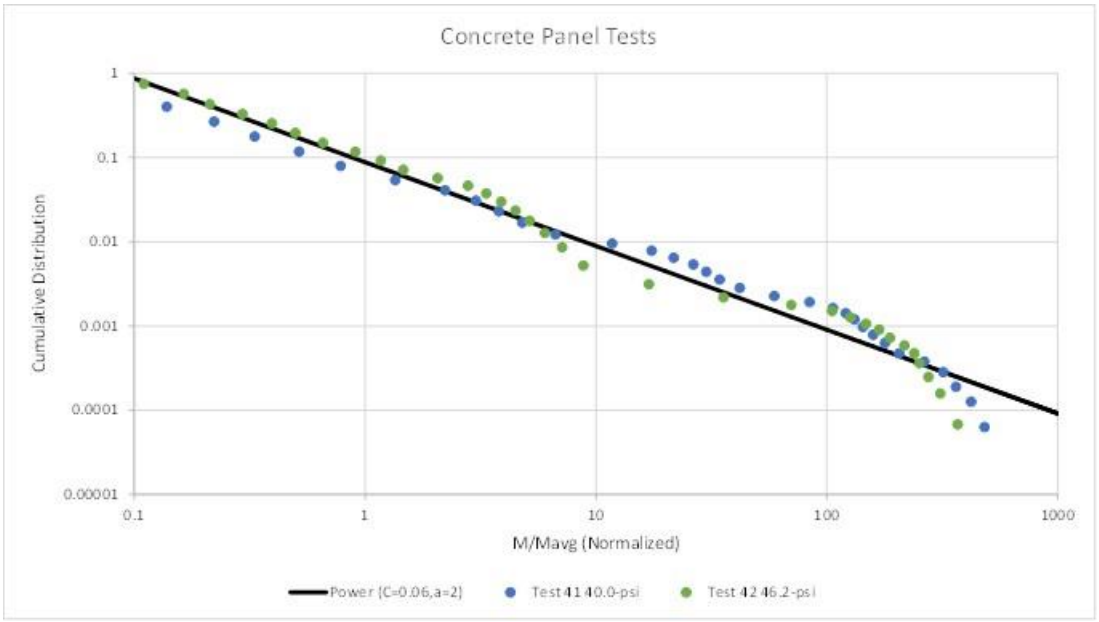

Figure 33. Best-fit power law mass distribution for physically-collected test data for PDF (top) and CDF (bottom) for Tests 41 and 42 involving concrete.

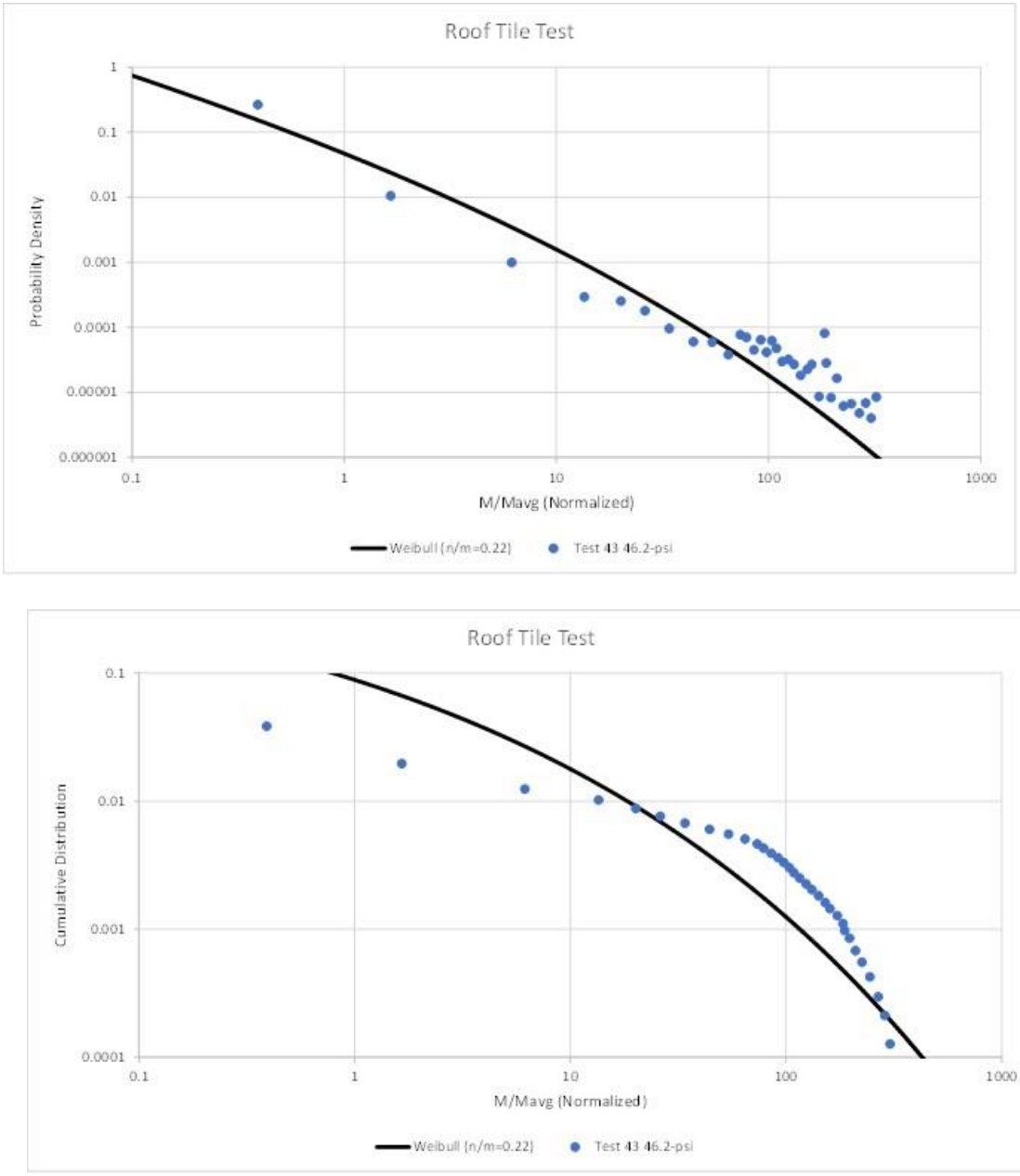

Figure 34. Best-fit Weibull mass distribution for physically-collected test data for PDF (top) and CDF (bottom) for Test 43 involving roof tile.

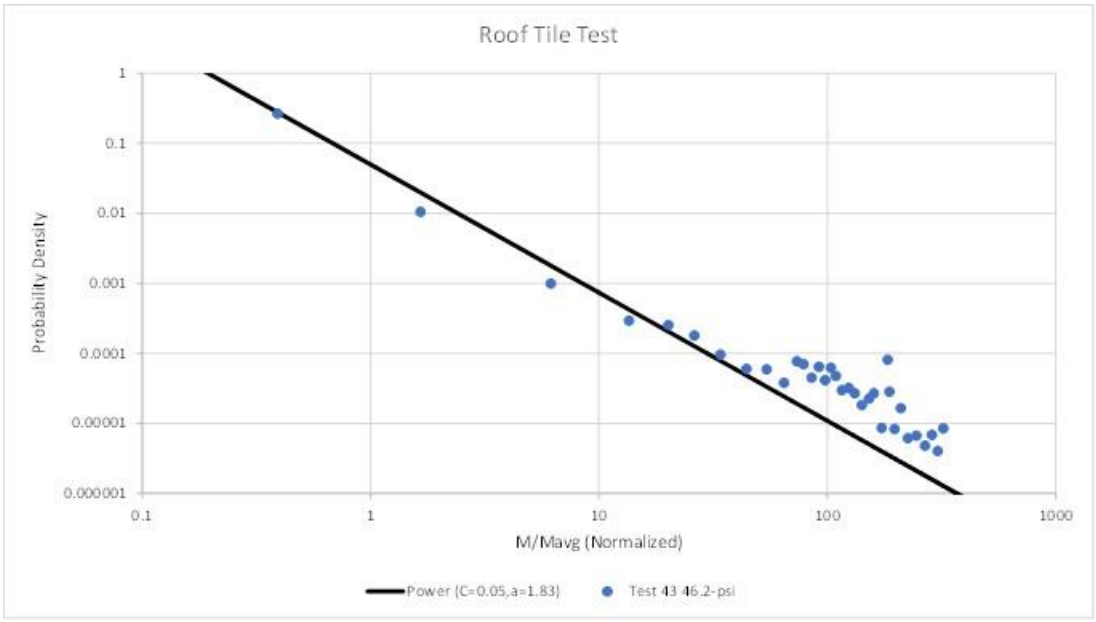

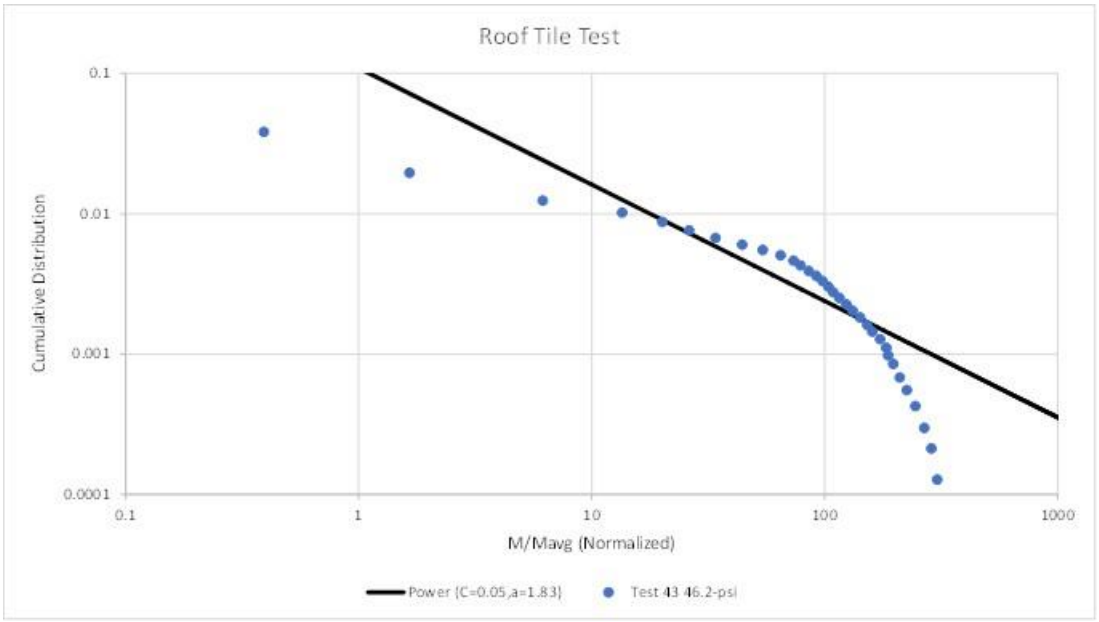

Figure 35. Best-fit power law mass distribution for physically-collected test data for PDF (top) and CDF (bottom) for Test 43 involving roof tile.

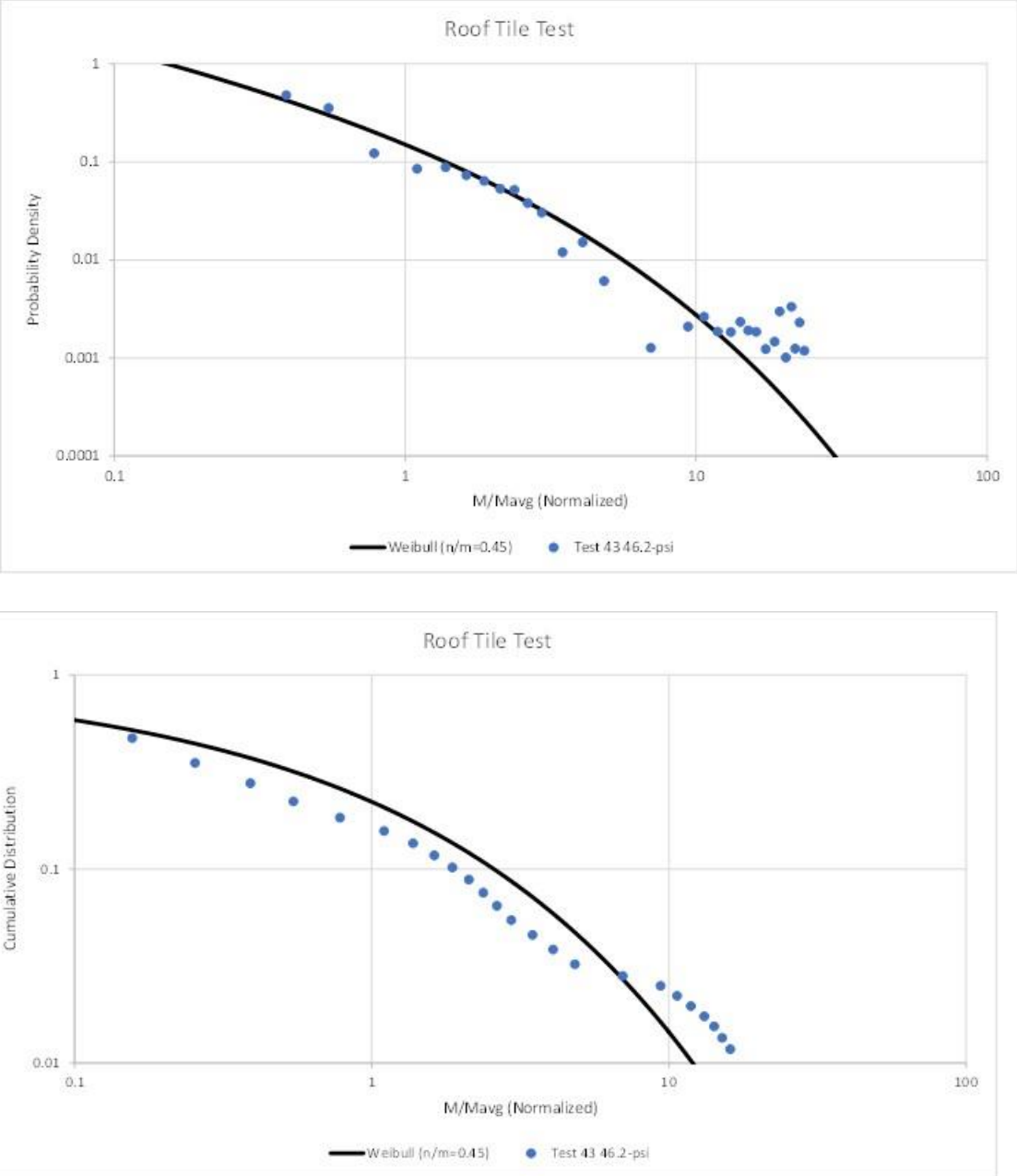

Figure 36. Best-fit Weibull mass distribution for physically-collected test data for PDF (top) and CDF (bottom) for truncated (<10 gram/small mass) distributions for Test 43 involving roof tile.

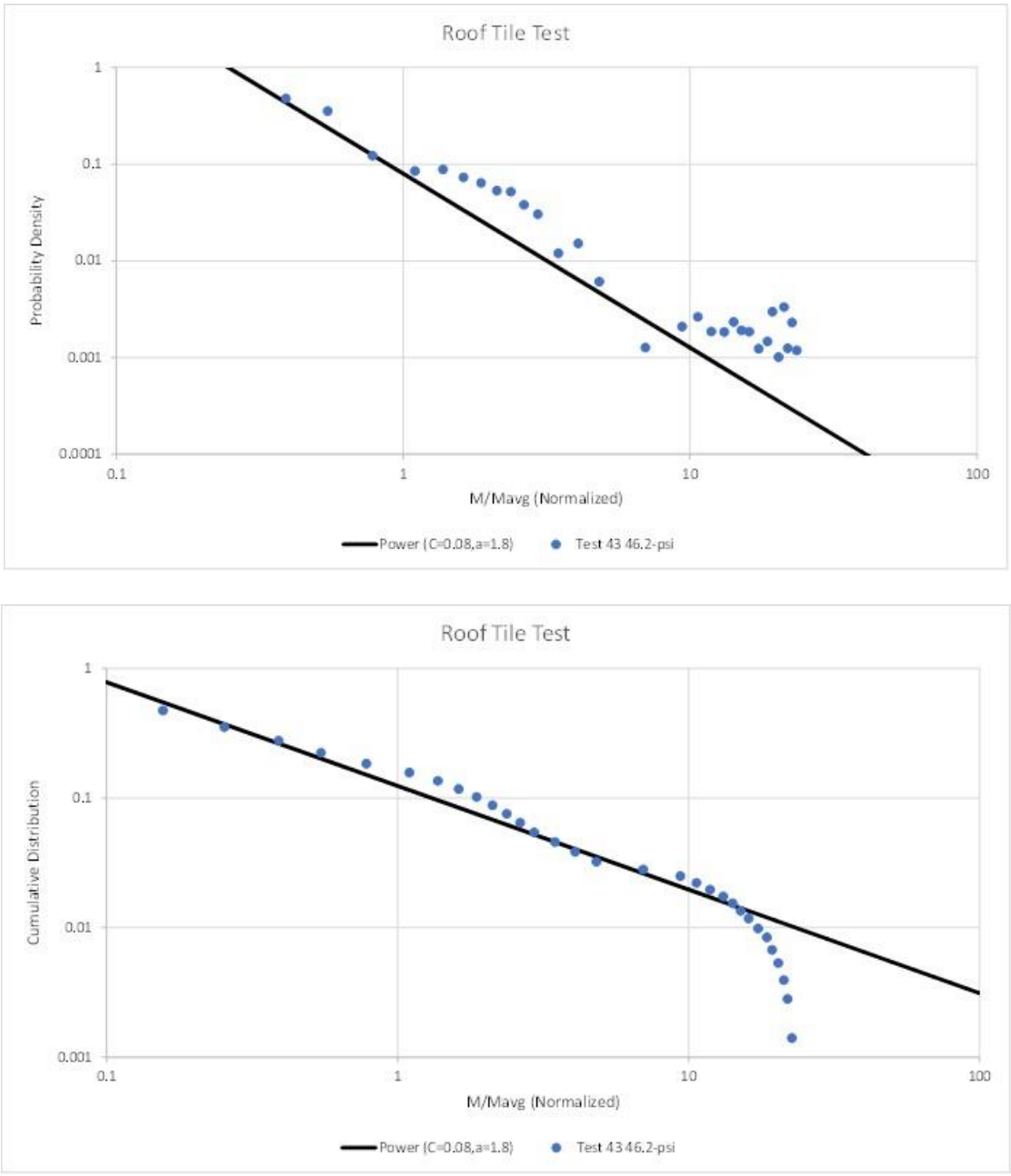

Figure 37. Best-fit power law mass distribution for physically-collected test data for PDF (top) and CDF (bottom) for truncated (<10 gram/small mass) distributions for Test 43 involving roof tile.

6 DISCUSSION

Fragments tend to form in two stages: a short initial stage dominated by rapid random crack formation and propagation; and an extended final stage dominated by high-speed collisions. In some cases, the initial stage determines the fragment size distribution. However, if shattering collisions are common enough, the final stage determines the fragment size distribution. The likelihood of shattering collisions depends on factors such as the following:

1. *Volumetric density*. For example, volumetric fragments density will be higher for thick objects like slabs than for thin objects like plates, leading to more mid-air collisions.
2. *Trajectory*. For example, chaotic three-dimensional fragment trajectories will lead to more mid-air collisions than diverging linear fragment trajectories.
3. *Speed*. Faster fragments will tend to shatter during collisions more often than slower fragments. Fragment speed depends on the applied load, elasticity, flexure, etc.
4. *Material strength*. For example, high-strength concrete fragments will tend to survive high-speed collisions better than weak annealed glass fragments.
5. *Adjacent hard surfaces*. High-speed fragments tend to shatter on impact with hard surfaces such as steel or concrete.

It is difficult to guess how these factors play out in any given scenario. For example, it might seem that plate glass windows are the most susceptible to mid-air collisions due their low strength. On the other hand, because plate glass is thin, the fragments tend to have a low volumetric density. In addition, because plate glass is weak, fragments tend to travel in diverging straight lines; see Figure 38. Both of these factors tend to minimize the number of collisions. However, glass fragments may still collide and shatter due to larger faster fragments (with less drag) overtaking smaller slower fragments (with more drag); see Figure 39.

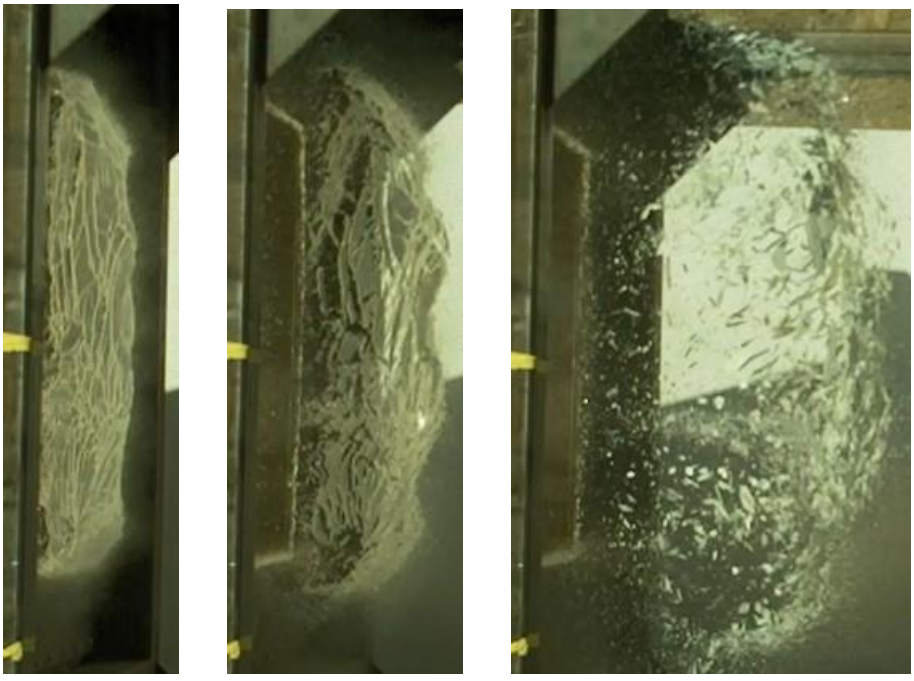

Figure 38. Early-time formation of fragments from a plate glass window in Test 17 [2].

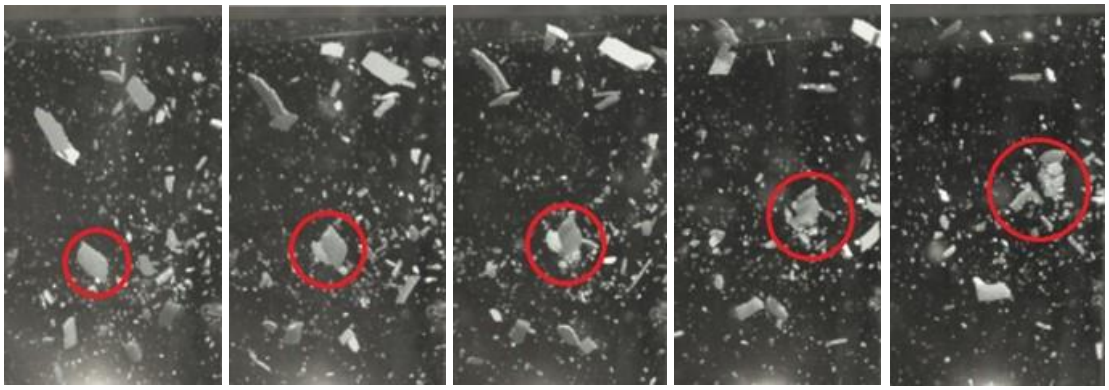

Figure 39. Mid-time evolution of fragments from a plate glass window due to shattering collisions in Test 17 [2].

For another example, it might seem that concrete is essentially impervious to most collisions, due its high strength. However, any event violent enough to break a slab of concrete into thousands of small pieces is also likely violent enough to severely damage those small pieces, e.g., cracks/splits, localized crumbling, and other macro- and microscopic defects that fall short of breakage; see, e.g., Fig. 15 in Reference [14] and Fig. 10 in Reference [15]. In other words, it might be a mistake to judge fragment strength based on virgin material. In addition, stronger materials can support higher applied loads prior to breaking. This means that, when those materials finally do break, their fragments potentially travel faster and in a more chaotic fashion than those from weaker materials at the same load; see, e.g., Fig. 18 in Reference [1].

To study the effects of fragment collisions, we previously attempted to measure fragment size distributions at early-, mid-, and late-times [1] [2] [3]. Unfortunately, in general, our tests captured only early-times or only late-times but not both. The exception was small-scale plate glass test samples [1] [3]. In those cases, comparing early- and late-time results, we found that the average fragment sizes decreased by factors of 10 or 20, which undoubtedly understates the true decrease, given the limitations on the smallest measurable fragments inherent with our techniques. Surprisingly, while the average fragment sizes changed, the fragment size distributions themselves did not change, except in extreme cases where the loads were unusually large or the glass strength was unusually small.

As indirect evidence of the effects of collisions, we compared the test results with and without a fragment stripper [1] [3]. The fragment stripper eliminated those fragments not traveling approximately perpendicular to the face of the original test sample. As a result, tests without the fragment stripper captured 5 to 15 times more fragments, both in terms of mass and number, than tests with the fragment stripper. More importantly, many fragments presumably collided with the sides of the fragment stripper. Fragments that shattered on, or ricocheted from, the sides of stripper presumably went on to collide with other fragments, leading to a collisional cascade ("chain reaction") that completely changed the outcome. Without the fragment stripper, the earlier concrete and CMU tests obtained a variety of different power law size distributions, in line with the results obtained the present series [3]. However, with the fragment stripper in place, concrete, and CMU tests obtained only a Weibull size distribution with $r \approx 2/3$ [1]. The fragment stripper had no effect on the size distribution for glass, either by happenstance, or because the initial glass fragments were much smaller than those for concrete and CMU, and thus were less likely to collide with the sides of the fragment stripper in a way that changed the outcome.

7 CONCLUSIONS

Table 7 and Table 8 summarizes the tests in Test Series 1, 2, 3, and 4. According to Table 7, when a Weibull size distribution was obtained, it was always the same Weibull size distribution with an exponent $r \approx 2/3$. However, according to Table 8, when a power law size distribution was obtained, the exponent varied in the range $r \approx -1 \pm 1/6$. The small-scales studied in Test Series 1 [1] and 3 [3] obtained similar results to the large-scales studied in Test Series 2 [2] and 4. Where differences exist, they probably relate more to sample thickness and loading than to scale.

Table 7. Tests in Test Series 1, 2, 3, and 4 that obtained Weibull size distributions based on physical collection.

Material	Tests	Ref.	Collision Metrics				Size Distribution	
			Sample Thickness	Strength	Load	Stripper Present	Type	Exponent
Temp. Glass	14, 15, 22	[1]	Thin (1/4")	Low	Low	Yes	Weibull	~2/3
	23, 24	[3]	Thin (1/4")	Low	Medium	No	Weibull	~2/3
Concrete	5, 6, 8, 9	[1]	Medium (2")	High	High	Yes	Weibull	~2/3
CMU	3, 4, 7, 10, 12	[1]	Medium (2")	High	High	Yes	Weibull	~2/3

Table 8. Tests in Test Series 1, 2, 3, and 4 that obtained power law size distributions based on physical collection.

Material	Tests	Ref.	Collision Metrics				Size Distribution	
			Sample Thickness	Strength	Load	Stripper Present	Type	Exponent
Temp. Glass	25, 39	[3]	Thin (1/4")	Low	High	No	Power Law	~ –1.08
Anneal. Glass	33, 34	[3]	Thin (1/4")	Very Low	Medium	No	Power Law	~ –5/6
Concrete	29, 30, 36, 38	[3]	Medium (1-2")	High	Medium to High	No	Power Law	~ –1
	41, 42	Table 6	Thick (4-5")	High	Very Low	No	Power Law	~ –1
CMU	31, 32, 35, 37	[3]	Medium (1.5-2")	High	Medium to High	No	Power Law	~ –7/6
	20	[2]	Thick (8")	High	Very Low	No	Power Law	~ –1
Brick	40	Table 6	Thick (3.5")	High	Very Low	No	Power Law	~ –5/6
Clay Tile	43	Table 6	Medium	High	Very Low	No	Power Law	~ –5/6

The rational Weibull exponent $r \approx 2/3$ given in Table 7 has been observed in numerous other studies. For example, Shi et. al. [16] studied low-yield explosive spalling damage to a 4-ft. x 5-ft. brick wall. By curve fitting their experimental results, they obtained a Weibull size distribution with $r \approx 1.33/2 = 0.665$. (This conversion from fragment diameter to mass assumes that most of the fragments formed in two-dimensions, i.e., that most of the fragments retained flat surfaces from the original brick wall, which is consistent with post-test photographs.) For another example, using maximum entropy theory, Liu et. al. [17] and Laney [18] derived a Weibull size distribution with $r = 2/3$.

Similarly, the rational power law exponents given in Table 8 have been observed in numerous other studies involving nearly steady, uniform conditions. For example, Schoutens [19] observed power laws with $r \approx -5/6$ in a large number of legacy cratering and ejecta tests involving large-scale nuclear detonations, high-explosive detonations, and high-velocity impacts. For another example, using mean-field theory for asteroid collisions, Dohnanyi [20] derived a power law size distribution with $r = -5/6$.

Traditionally, power laws are associated with brittle fragmentation (e.g., concrete, ceramics, glass, brick, rock, masonry) while Weibull size distributions are associated with ductile fragmentation (e.g., metals, plastics, melts). However, our tests found that glass, a classically brittle material, often obtains a Weibull size distribution [1] [2] [3]. The real distinction may be not ductile versus brittle, but the number and type of shattering collisions. Brittle materials, such as those studied here, tend to be damaged during fragmentation, leaving them vulnerable to shattering during collisions. By contrast, ductile materials tend to be distorted rather than damaged during fragmentation, leaving them resistant to shattering during collisions. This distinction may matter less for thin materials, like plate glass, that form low-volumetric-density clouds that do not allow for frequent mid-air collisions.

8 REFERENCES

[1] B. Bewick, G. Rolater, J. Bui, M. Barsotti, K. Marchand, A. Ziemba, M. Sanai and C. Laney, "Fragmentation of Solid Materials Using Shock Tubes. Part 1: First Test Series in a Small-Diameter Shock Tube," DTRA-TR-17-21, 2017.

[2] B. Bewick, G. Rolater, K. Marchand, A. Ziemba, M. Sanai and C. Laney, "Fragmentation of Solid Materials Using Shock Tubes. Part 2: First Test Series in a Large-Diameter Shock Tube," DTRA-TR-17-50, 2017.

[3] B. Bewick, G. Rolater, K. Marchand, A. Ziemba, M. Sanai and C. Laney, "Fragmentation of Solid Materials Using Shock Tubes. Part 3: Second Test Series in a Small-Diameter Shock Tube.," DTRA, 2018.

[4] R. A. Keys and S. K. Clubley, "Experimental Analysis of Debris Distribution of Masonry Panels Subjected to Long Duration Blast Loading," *Engineering Structures,* vol. 130, pp. 229-241, 2017.

[5] R. V. Johns and S. K. Clubley, "The Influence of Structural Arrangement on Long-Duration Blast Response of Annealed Glazing," *International Journal of Solids and Structures,* Vols. 97-98, pp. 370-388, 2016.

[6] R. V. Johns and S. K. Clubley, "Experimentally Investigating Annealed Glazing Response to Long-Duration Blast," *Journal of Structural Engineering,* vol. 143, no. 11, 2017.

[7] R. A. Keys and S. K. Clubley, "Establishing a Predictive Method for Blast Induced Masonry Debris Distribution using Experimental and Numerical Methods," *Engineering Failure Analysis,* vol. 82, pp. 82-91, 2017.

[8] I. G. Bowen, M. E. Franklin, E. R. Fletcher and R. W. Albright, "Secondary Missiles Generated by Nuclear-Produced Blast Waves," USAEC Civil Effects Test Group Report WT-1468, October 1963.

[9] J. S. Davidson, J. M. Hoemann, J. S. Shull, R. J. Dinan, H. A. Salim, B. T. Bewick and M. I. Hammons, "Full-scale Experimental Evaluation of Partially Grouted, Minimally Reinforced Concrete Masonry Unit (CMU) Walls Against Blast Demands," AFRL-RX-TY-TR-2011-0025-01, November 2010.

[10] M. I. Hammons, B. T. Bewick and J. S. Davidson, "Full-Scale Blast Test Response of Partially Grouted Masonry Walls," AFRL-RX-TY-TP-2011-0007, January 2011.

[11] L. M. Vargas and J. C. Hokanson, "Explosive Fragmentation of Dividing Walls," ARLCD-CR-81018, 1981.

[12] R. L. Barnett and P. C. Hermann, "Fragmentation of Reinforced Concrete Slabs," IIT Research Institute Final Report for Project J6107, October 1968.

[13] M. Sanai, H. I. Lindberg and J. D. Colton, "Simulation of Blast Waves with Tailored Explosive Charges," *Journal of Fluid Mechanics,* vol. 158, pp. 137-152, 1984.

[14] J. D. Hogan, J. G. Spray, R. J. Rogers, G. Vincent and M. Schneider, "Dynamic Fragmentation of Natural Ceramic Tiles: Ejecta Measurements and Kinetic Consequences," *International Journal of Impact Engineering,* vol. 58, pp. 1-16, 2013.

[15] F. Sommer, F. Reiser, A. Dufresne, M. H. Poelchau, T. Hoerth, A. Deutsch, T. Kenkmann and K. Thoma, "Ejection Behavior Characteristics in Experimental Cratering in Sandstone Targets," *Meteoritics & Planetary Science,* vol. 48, no. 1, pp. 33-49, 2013.

[16] Y. Shi, W. Xiong, Z.-X. Li and Q. Xu, "Experimental Studies on the Local Damage and Fragments of Unreinforced Masonry Walls under Close-In Explosions," *International Journal of Impact Engineering,* vol. 90, pp. 122-131, 2016.

[17] Y. Liu, "On the Generalized Theory of Atmospheric Particle Systems," *Advances in Atmospheric Sciences,* vol. 12, no. 4, pp. 419-438, 1995.

[18] C. B. Laney, "Effects of Mixtures on Liquid and Solid Fragment Size Distributions," DTRA-TR-16-52, May 2016.

[19] J. E. Schoutens, Nuclear Geoplosics Sourcebook, Volume IV, Part II: Empirical Analysis of Nuclear and High-Explosive Cratering and Ejecta, Washington DC: Defense Nuclear Agency, 1979.

[20] J. S. Dohnanyi, "Collisional Model of Asteroids and their Debris," *Journal of Geophysical Research,* vol. 74, no. 10, p. 2531–2554, 1969.